Precambrian Research 369 (2022) 106507

Contents lists available at ScienceDirect

Precambrian Research

journal homepage: www.elsevier.com/locate/precamres

Multistage petrogenetic evolution of Neoproterozoic serpentinized ultramafic rocks and podiform chromitites at Hagar Dungash, Eastern Desert of Egypt

Hilmy E. Moussa [a], Heba S. Mubarak [a], Mokhles K. Azer [a,*], Adel A. Surour [b,c], Paul D. Asimow [d], Mona M.L. Kabesh [b]

[a] Geological Sciences Department, National Research Centre, 12622 Dokki, Cairo, Egypt
[b] Department of Geology, Faculty of Science, Cairo University, 12613 Giza, Egypt
[c] Department of Geological Sciences, Faculty of Science, Galala University, 43511 New Galala City, Egypt
[d] Division of Geological & Planetary Sciences, California Institute of Technology, Pasadena, CA 91125, USA

ARTICLE INFO

Keywords:
Gabal Hagar Dungash
Dismembered ophiolite
Chromitite ore
Kämmererite
Fore-arc mantle peridotite
Supra-subduction zone

ABSTRACT

Podiform chromitites are found in the mantle sections of ophiolites in many places and times in the geologic record. Leading theories for their origin invoke melt-rock reaction processes involving hydrous melts in supra-subduction zone settings. Here we develop a case study of a Neoproterozoic example and a quantitative thermodynamic model of the multistage process leading to nearly monomineralic chromitite pods. We demonstrate that the Hagar Dungash ophiolite of the Eastern Desert of Egypt — despite being dismembered, incomplete, and affected by variable degrees of alteration and metamorphism — is nevertheless plainly a supra-subduction zone ophiolite containing podiform chromitite deposits. Textural, mineralogical, and chemical evidence from the serpentinized ultramafic rocks point to mantle protoliths residual to high degrees of partial melt extraction, characteristic of fore-arc ophiolites. The chromitite pods are distinguished into massive and nodular types; Cr-spinel in the massive type is almost fresh, with intermediate to high Cr# (0.60–0.85) and extremely low Fe^{3+}# (nil-0.04). Cr-chlorite with up to ~ 15 wt% Cr_2O_3 is a common interstitial mineral in the chromitites. The observations are consistent with the conceptual multistage model wherein boninitic melt develops as the end-product of melt-harzburgite reaction in the shallow upper mantle. Mixing between this boninitic melt and ascending peridotite-derived basaltic melt drives the liquid deep into the Cr-spinel stability field and precipitates nearly monomineralic chromitite. Our thermodynamic model of this mixing and precipitation process reproduces the mineral chemistry trends of the fresh chromite samples and yields an estimate of the efficiency of chromite production relative to melt flux through the system, which can be applied to development of podiform chromitites in supra-subduction systems worldwide and across geologic eras.

1. Introduction

The ultramafic members of ophiolite sequences have proven to be critical sources of information for understanding geodynamic and tectonomagmatic processes in ancient ocean basins (e.g., Dilek et al., 2008; Dilek and Thy, 2009; Dilek and Furnes, 2011, 2014; Gahlan et al., 2021). Among the diagnostic lithologies found in these sequences, much attention has focused on chromitite deposits — both for their economic value and for the strong constraints on chemical sources and petrogenetic processes that arise from their characteristics. In general, chromitite ores occur as podiform masses in residual mantle peridotites and as stratiform layers in ultramafic cumulate sequences (Jackson and Thayer, 1972). Here we focus on the origin of podiform chromitites. Where field relations are well-preserved, podiform chromitites occur as discontinuous lensoidal bodies with sharp contacts, commonly surrounded by envelopes of dunite, within ophiolitic harzburgite outcrops (Miura et al., 2012; Khedr and Arai, 2017; Arai and Yurimoto, 1994; Gahlan et al., 2020b). The podiform chromitites of various sizes and shapes in the shallowest parts of the ophiolitic ultramafic sequences in the Eastern Desert of Egypt commonly follow this pattern, whether they

* Corresponding author.
E-mail address: mk.abdel-malak@nrc.sci.eg (M.K. Azer).

https://doi.org/10.1016/j.precamres.2021.106507
Received 22 March 2021; Received in revised form 2 December 2021; Accepted 3 December 2021
Available online 28 December 2021

are massive or granular (nodular) and whether they are concordant or discordant with the fabric of surrounding peridotites (e.g., Abu El Ela and Farahat, 2010; Khedr and Arai, 2017; Azer et al., 2019; Ali et al., 2020a).

Podiform chromitites may be found in a variety of tectonic settings and their genesis and mechanism of Cr concentration has been the subject of much discussion in the literature (e.g., Lago et al., 1982; Roberts, 1988; Arai and Yurimoto, 1994; Zhou et al., 1994; Arai, 1997; Zhou and Robinson, 1997; Matveev and Balhaus, 2002; Rollinson, 2005; Morishita et al., 2006; Yang et al., 2015; Arai and Miura, 2016; Griffin et al., 2016; Habtoor et al., 2017; Khedr and Arai, 2017; Xiong et al., 2017; Wu et al., 2019; Abuamarah et al., 2020). The hypotheses for the genesis of podiform chromitites can be broadly grouped into four categories: 1) podiform chromitites, rich in compatible elements and found in residual mantle sequences, may represent part of the mantle residue after extensive melt extraction; 2) some podiform chromitites are thought to be derived from the deep mantle due to the presence of ultra-high pressure mineral phases (e.g., Yamamoto et al., 2009; Yang et al., 2015; Griffin et al., 2016; Wu et al., 2019); 3) podiform chromitites may be cumulates deposited in magma conduits through residual mantle; and 4) podiform chromitites may form by processes of melt/rock interaction associated with melt transport through the upper mantle. A successful model must offer an explanation for the production of abundant, nearly monomineralic chromitite, without concomitant crystallization of other phases (Zhou et al., 2005).

In recent years, most authors have adopted a model of melt-peridotite interaction followed by melt mixing to drive the system to chromite saturation and precipitate podiform chromitites in the uppermost mantle (González-Jiménez et al., 2011; Arai and Miura, 2016; Khedr and Arai, 2017; Azer et al., 2019; Abuamarah et al., 2020; Gahlan et al., 2021). In the melt-rock interaction and melt mixing mechanism, ascending basaltic melts react with overlying peridotites. This process dissolves orthopyroxene and spinel, precipitating olivine to produce a dunite envelope and a modified boninitic melt rich in Si and Cr. However, once orthopyroxene is exhausted from the conduit, later ascending melts do not undergo this reaction and reach low pressure while retaining low-Si compositions. Mixing of the early reacted melt with the new influx of primitive melt drives the melt to a composition that is saturated only with Cr-spinel on the liquidus. A certain volume of monomineralic chromitite may then be precipitated before the melt once again becomes saturated with olivine (Arai and Abe, 1995; Roberts, 1988). The presence of dunite envelopes surrounding most of the Egyptian podiform chromitites (e.g., Ahmed et al., 2001; Abu El Ela and Farahat, 2010; Ahmed, 2013; Khedr and Arai, 2016, 2017) favors such wall-rock interaction and melt-mixing mechanisms for their formation (e.g., Lago et al., 1982; Paktunc, 1990; Arai and Yurimoto, 1994; Zhou et al., 1996, 2005; Arai, 1997; González-Jiménez et al., 2014), since exhaustion of orthopyroxene from the conduit is a necessary feature of the process.

In broad outline, chromitite formation by the melt-rock interaction and mixing mechanism may occur in any tectonic environment where ascending melts react with harzburgite residues, and differences among podiform chromitites may reflect variations in parameters like melt-rock ratio as well as different tectonic settings (Edwards et al., 2000; Khedr and Arai, 2017; Matveev and Balhaus, 2002). Nonetheless, large-scale and abundant chromitite pods are much more often recorded in supra-subduction zone (SSZ) settings than in mid-ocean ridge settings (Zhou et al., 1994; Arai, 1997; Arai and Matsukage, 1998). The large flux of slab-derived fluids or melts and the large volume of highly refractory harzburgites in the SSZ environment both facilitate the rock-melt interactions that lead to chromitite formation (Melcher et al., 1999; Edwards et al., 2000; Matveev and Balhaus, 2002; Mondal et al., 2006; Uysal et al., 2007, 2016). There is most likely a link between high water content and the concentration of Cr by melt-peridotite reaction (Edwards et al., 2000; Khedr and Arai, 2017; Azer et al., 2019; Gahlan et al., 2021).

Although the SSZ melt-rock reaction scenario for podiform chromitite formation has been developed through a series of detailed observational studies and has some experimental support, key aspects of the concept remain to be constrained. In particular, the coupled mass and energy balances that limit the efficiency of chromitite production (per unit melt flux) call for a thermodynamic model. In this work, we first develop a case study from the Hagar Dungash (HD) area of the Eastern Desert of Egypt. The volcano-sedimentary successions exposed in the area are well known due to gold mineralization in the so-called "Dungash Mine Area". Hence, most published studies of the area have focused on the genesis of the gold and petrological aspects of the arc-related volcano-sedimentary host rocks (e.g., Khalid et al., 1987; Helba et al., 2001; Khalil et al. 2003; Zoheir et al., 2008; Zoheir and Weihed, 2014; Kassem and Abd El Rahim, 2014; Kassem et al., 2016; Salem et al., 2016; Dourgham et al. 2017). The study of Abu El Ela and Farahat (2010) presents mineral chemistry data from the massive chromitite pods in the area, however none of these papers includes whole-rock analyses, detailed information about the serpentinized peridotites of the HD area, or a full description of the two varieties of associated chromitite ore. We focus on characteristics of ultramafic samples that are robust despite metamorphism and alteration, in order to establish that the HD ophiolite has an SSZ character and that it contains podiform chromitites whose mineral chemistry can be well characterized. Then we apply the quantitative thermodynamic model of podiform chromitite genesis first introduced in Abuamarah et al. (2020) to our observations of the HD chromitite pods and their host serpentinite rocks. We show that the model not only explains the occurrence of nearly monomineralic chromitite but also provides a good fit to the mineral chemistry observations, lending additional confidence to the use of the model to define the efficiency of chromitite genesis and therefore the theoretical upper bound on the size of such deposits.

2. Geologic setting

In the Neoproterozoic Arabian-Nubian Shield (ANS), the northern part of the East African Orogen, ophiolite sequences have yielded important clues about the origin and evolution of the shield (Abuamarah, 2019; Gahlan et al., 2021; Moussa et al., 2021). Broadly speaking, ophiolites, serpentinites, and ophiolitic mélange decorate suture zones throughout the ANS — in Saudi Arabia, the Eastern Desert of Egypt, and northeastern Sudan. These sutures mark locations where terranes were accreted during the amalgamation of the ANS as the Mozambique Ocean closed (e.g., Pallister et al., 1988; Dilek and Ahmed, 2003; Stern et al., 2004; Johnson et al., 2004; Azer and Stern, 2007) in events that allowed oceanic crust to be obducted and tectonically emplaced onto continental margins.

Ophiolites make up a volumetrically minor, but tectonically important, component of the Neoproterozoic rocks in the central and southern parts of the Egyptian Eastern Desert (Fig. 1). They occur as tectonized, dismembered bodies and mélanges that comprise variably metamorphosed ultramafic rocks (such as serpentinite, serpentinized peridotite, and metapyroxenite) as well as mafic crustal units (such as metagabbro, sheeted metadiabase, and pillowed metabasalts). In some instances, the serpentinites preserve sporadic outcrop-scale relics of fresh peridotite and dunite. Due to folding, faulting, shearing, and voluminous later intrusive activity, most ophiolites in the Eastern Desert are incomplete, lacking one or more diagnostic lithology. Without exception, the Egyptian ophiolites are strongly deformed, metamorphosed and metasomatically altered by processes such as silicification, chloritization and carbonation (Abdel-Karim et al., 2021a, Moussa et al., 2021). The ophiolitic ultramafic rocks in the Eastern Desert of Egypt host numerous important mineral deposits, including magnesite, chromitite, talc and gold (Klemm et al., 2001; Kusky and Ramadan, 2002; Azer, 2013; Boskabadi et al., 2017). This understudied component of the local geology provides context for the later island-arc stage while also helping to define the tectonic evolution and metamorphic history

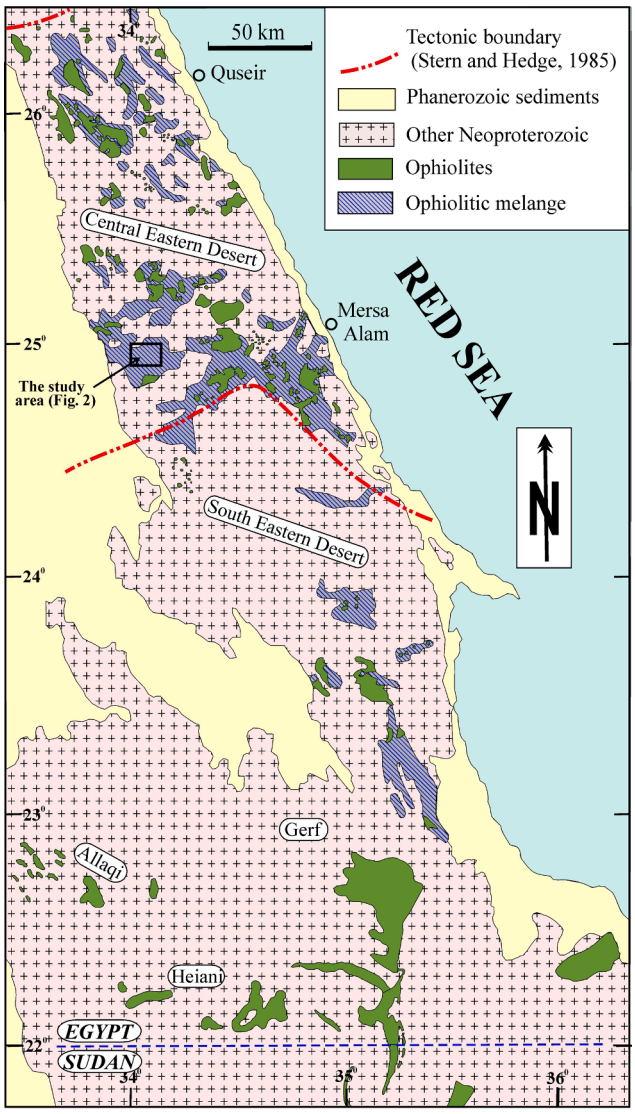

Fig. 1. Distribution of ophiolites in the Eastern Desert of Egypt (modified after Shackleton, 1994). Location of the study area (Fig. 2) is indicated.

(including metasomatism) of accreted oceanic lithosphere in the Eastern Desert of Egypt.

The HD area is located near the western boundary of the basement exposures of the Central Eastern Desert of Egypt. It is bounded by longitudes 33° 47′ & 34° 00′ E and latitudes 24° 52′ & 25° 00′ N, in the southern part of the El-Barramiya district. It lies on the southern side of the Idfu-Mersa Alam road, almost midway between Mersa Alam on the Red Sea and Idfu on the River Nile. The Neoproterozoic rocks exposed in the study area comprise a dismembered ophiolite, an island-arc volcano-sedimentary sequence, a metagabbro-diorite complex, granodiorite, monzogranite and a fresh gabbro (Fig. 2). In places, the Neoproterozoic rocks are covered non-conformably by Phanerozoic clastic rocks (Nubian-facies sandstones) and dissected by various wadis. The ophiolitic rocks constitute up to 35% of the total mapped area. They represent obducted slices of ancient oceanic lithosphere, emplaced over the island-arc succession with a tectonic contact. The ophiolitic rocks include serpentinite, serpentinized dunite and peridotite, chromitite (in lenses, now mostly mined out), and metagabbro. The ultramafic rocks are variably serpentinized and may show other types of metasomatic alteration. The serpentinites vary in colour but most are black or greenish-black. Ultramafic outcrops vary from large, massive sheet-like bodies (Fig. 3**a**) in the northern part of the mapped area to small hillocks confined to the southeastern part. Most serpentinite sheets are elongated in a general ENE-WSW to E-W direction. In the largest serpentinite masses, NNW-dipping imbricate thrust sheets are observed. Deformation along local shear zones and fault planes has resulted in foliated schistose serpentinites that may be brecciated along fracture systems conjugate to the shear direction. Locally, penetrative foliation and mylonitization can be observed. Both deformed and undeformed quartz and carbonate veins are common, elongated in a NW-SE direction. Talc-carbonate rocks are common; they form yellowish-white to greenish-cream cavernous masses (Fig. 3**b**) that contrast strongly with the darker mafic and ultramafic units. Talc-carbonate is most abundant in the northwestern corner of the HD area, close to the peak of Gabal Dungash.

Chromitite is hosted by serpentinized peridotites. This Cr-ore occurs in the form of pods or lenticular podiform bodies from ~ 0.5–1 m wide (Fig. 3**c**). The pods are concordant to the foliation of the serpentinite host and are typically elongated parallel to the E-W trend of the serpentinite belt. Both at outcrop and thin-section scales, the chromitite pods may be either massive or sheared. To a large extent, they have been excavated or mined out. Where contacts between serpentinite and chromitite can still be observed, most contacts are relatively sharp but diffuse boundaries can also be found. Magnesite ore is found as hard, massive, snow-white (or iron-stained) veins with sharp but irregular contacts against serpentinite (Fig. 3**d**). Such veins are generally sparse, but they become more concentrated near the basal contact of the ophiolite and along regional faults.

3. Petrography

On a petrographic basis, the ophiolitic ultramafic rocks in the HD area are mainly serpentinized peridotite and chromitite. The serpentinized peridotite is distinguished into massive, sheared, and carbonated varieties. Their mineralogical and textural variations preserve indications of their igneous, metamorphic, and structural history.

3.1. *Massive serpentinite*

The massive serpentinite consists essentially of serpentine minerals (antigorite, lizardite and chrysotile, >90% of the rock volume) together with variable amounts of talc, amphibole, carbonate and opaque minerals. Fresh pyroxene and Cr-spinel relics are recorded in some samples along with very scarce and very small relics of fresh olivine. Pseudomorphic textures after primary minerals are common; most massive serpentinite samples are dominated by bastite and mesh textures (Fig. 4**a, b,** respectively). In other samples, textural evidence of primary mineralogy has been partly or totally erased in favor of serpentine minerals occurring as aggregates of plates and plumose fibers with interlocking to interpenetrating fabrics (Fig. 4**c**). Cross-fiber veinlets of chrysotile are observed traversing an antigorite-dominated matrix. Some of the antigorite and lizardite occur as elongated crystals clustered into bundles (note, petrographic serpentine mineral identification was verified by Raman spectroscopy, see below). Opaque minerals are represented mainly by Cr-spinel, magnetite and a few tiny sulphides (mostly chalcopyrite and pentlandite). Cr-spinel occurs as subhedral to euhedral disseminated crystals that display deep reddish-brown colour in thin-section under plane-polarized light. The majority of Cr-spinel is partly replaced by rims of ferritchromite and irregular overgrowths of magnetite (Fig. 4**d**). Patches, sparse crystals and fine aggregates of carbonate are mainly magnesite with much less dolomite. Some samples contain minor talc and fibrous or columnar aggregates of tremolite and actinolite formed at the expense of talc and serpentine.

3.2. *Carbonated serpentinite*

Some samples of serpentinite are rich in carbonates; we label these “carbonated serpentinites”. Mineralogically, they consist of serpentine minerals (~65–80%) and carbonates, mostly magnesite (~15–30%)

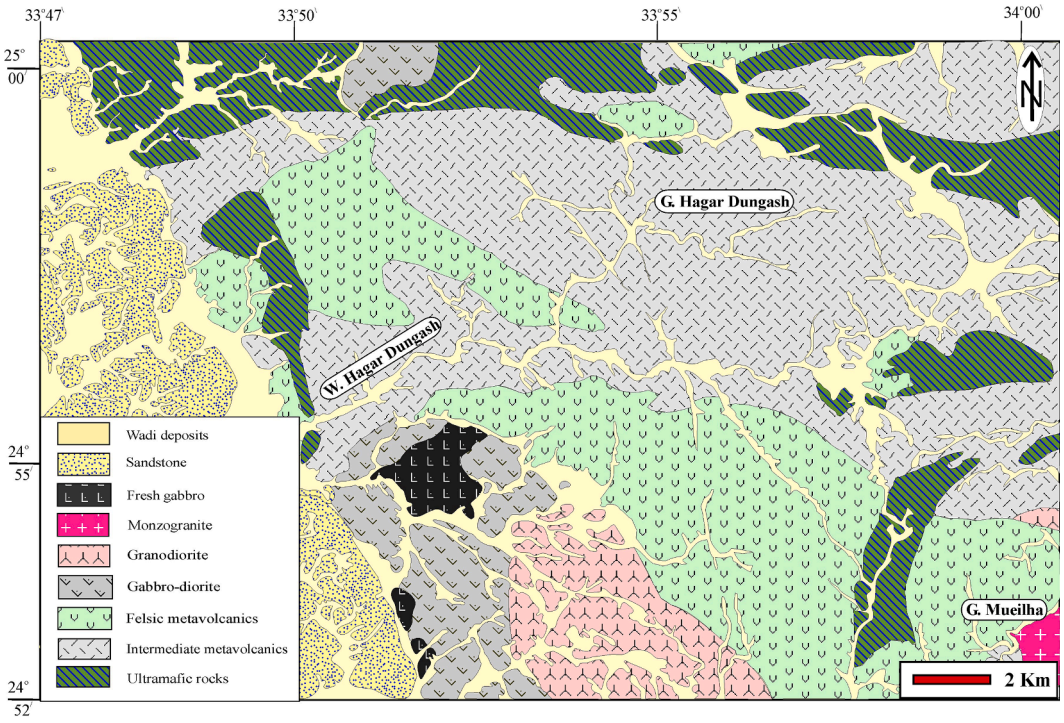

Fig. 2. Geological map of the Hagar Dungash area, modified after Hussein et al. (1996).

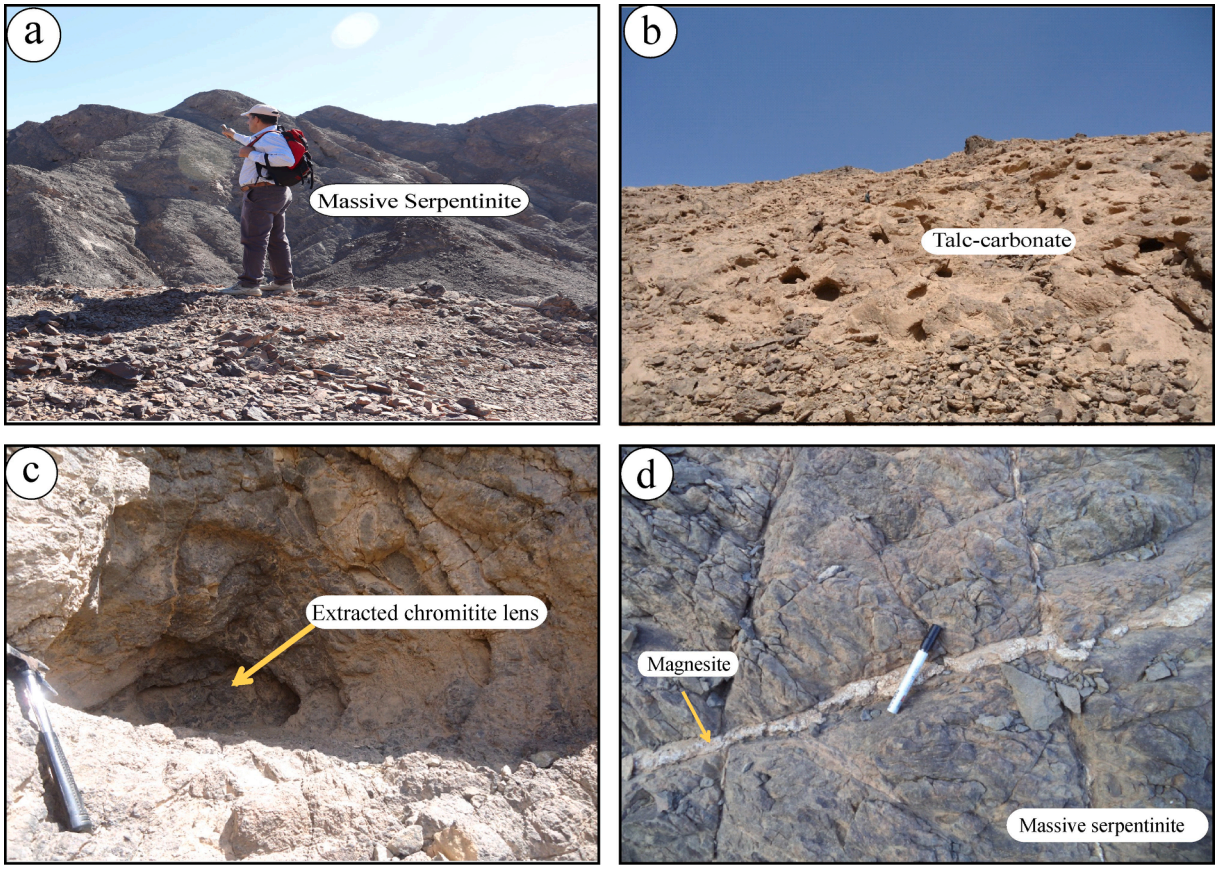

Fig. 3. Field photographs: (a) massive sheet-like body of serpentinite, (b) cavernous weathering in talc-carbonate rocks (note geologist at upper center of image for scale), (c) excavated lenticular chromitite body, and (d) snow-white magnesite vein cutting massive serpentinite.

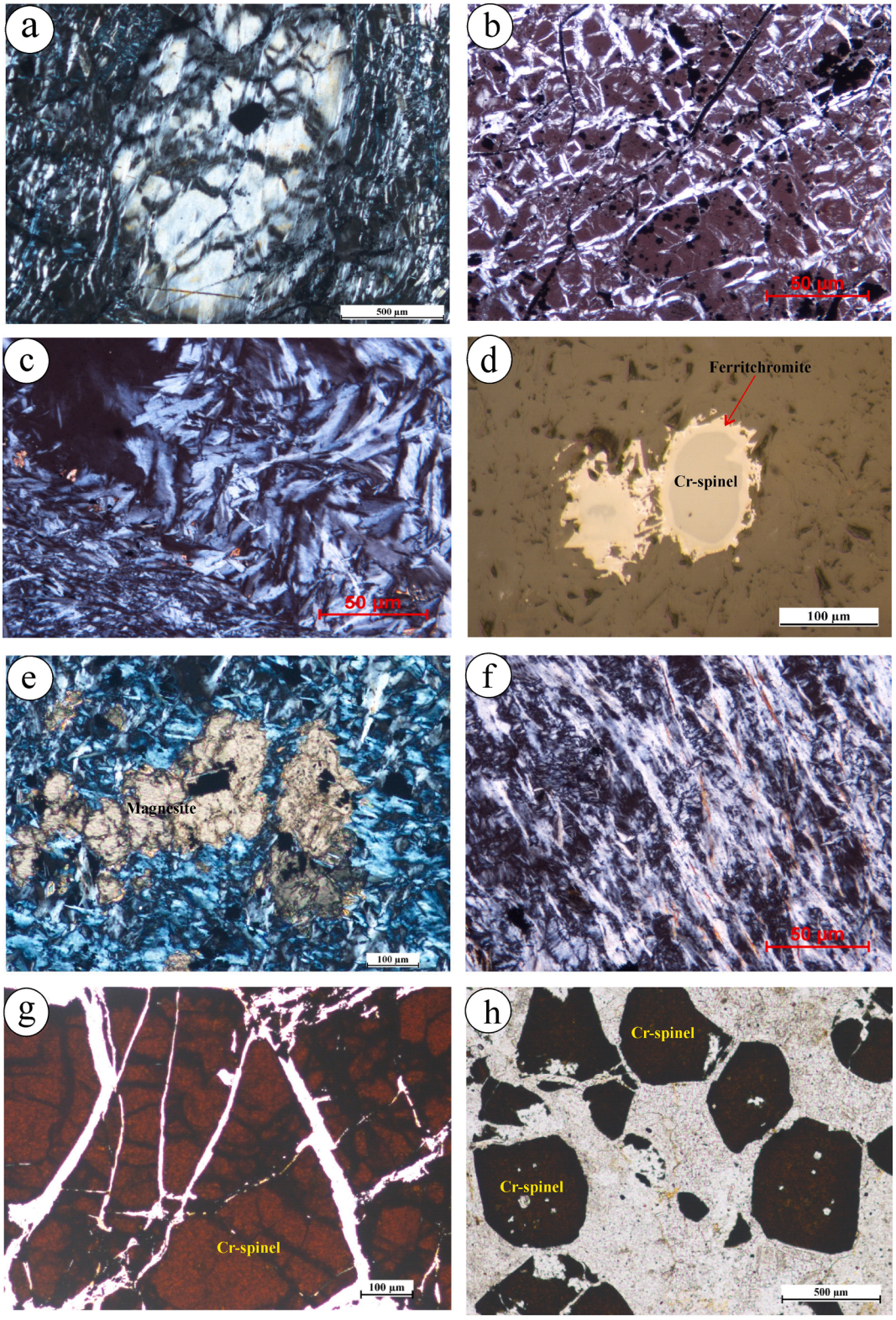

Fig. 4. Petrographic images: (a) bastite texture in massive serpentinite, (b) mesh texture in massive serpentinite, (c) fibrous aggregate of serpentine minerals in massive serpentinite, (d) Cr-spinel with rims partly replaced by ferritchromite and Cr-magnetite in massive serpentinite, (e) serpentine minerals intergrown with magnesite in carbonated serpentinite, (f) sub-parallel alignment of serpentine flakes producing schistosity in sheared serpentinite, (g) reddish brown coarse cracked crystals of Cr-spinel in massive chromitite, and (h) Cr-spinel crystals disseminated in a silicate matrix in nodular chromitite. Images (a), (b), (c), (e), and (f) are taken in cross-polarized transmitted light. Images (g) and (h) are taken in plane-polarized transmitted light. Panel (d) is taken in reflected light.

with accessory talc, Cr-spinel, and magnetite. The serpentine minerals occur as flame-like crystals that exhibit some interpenetrating texture. Coarse antigorite crystals are intergrown with magnesite (Fig. 4**e**). Magnesite forms fine aggregates and discrete crystals that are occasionally Fe-stained, and intersecting veinlets. Talc occurs as coarse flakes or as fine crystals associated with coarse antigorite and magnesite. Cr-spinel forms subhedral to anhedral crystals. Along grain boundaries and cracks, Cr-spinel is partly replaced by an irregular ferritchromite zone and an outer Cr-magnetite rim.

3.3. Sheared serpentinite

Sheared serpentinite is similar in mineralogical composition to massive serpentinite, but the sheared variety lacks pseudomorphs and expresses a schistosity defined by subparallel alignment of serpentine flakes (Fig. 4**f**). Antigorite is the main mineral, with lesser amounts of chrysotile, lizardite, magnesite, talc, chlorite, brucite, Cr-spinel and magnetite. No fresh relics of primary silicate minerals are observed. Fractures in the sheared serpentinites are filled with chrysotile, quartz, carbonate minerals, and veinlets of chlorite and brucite. Brucite has been observed in fully-replaced serpentinites in other ANS ophiolite localities (Um Rashid, Mubarak et al., 2020; Abuamarah et al., 2020), despite the expectation that brucite will react away quickly once olivine is exhausted from the mineral assemblage buffering the fluid chemistry (Bach et al., 2004). Highly brecciated Cr-spinel is the only surviving primary mineral. It occurs as small subhedral to anhedral crystals or as chain-like trails of subhedral crystals. Primary dark brown or deep red Cr-spinel is partially altered along cracks and grain boundaries to ferritchromite and Cr-magnetite.

3.4. Chromitite

Two types of podiform chromitites are recognized in the HD area: massive and nodular. Both types are hosted in massive serpentinite. Massive chromitite is mostly fresh and composed mainly of Cr-spinel (>90%) with minor silicate minerals found interstitially and in cracks. The interstitial minerals include serpentine minerals, carbonates and minor chlorite. Very small inclusions of silicate minerals are observed within Cr-spinel. Reddish-brown Cr-spinel forms subhedral to anhedral coarse cracked crystals exhibiting pull-apart texture (Fig. 4**g**). Almost all the Cr-spinel is fresh, although slight alteration of boundaries to ferritchromite can be found. Cumulate, chain structures, and banding are common textures in the massive chromitite and are typical of magmatic crystallization (Pal and Mitra, 2004). Small grains of Cr-bearing chlorite, confirmed by the electron microprobe, are enclosed within Cr-spinel, or found interstitially or in thin veinlets.

The nodular chromitite consists of Cr-spinel (40–60 vol%) with subordinate carbonate minerals, serpentine minerals, chlorite and opaques. In this variety, the majority of Cr-spinel crystals (0.5–1 cm in length) are subhedral to euhedral. The crystals are smaller than those in the massive chromitite (Fig. 4**h**). Some crystals exhibit pull-apart texture with cracks filled by serpentine minerals, carbonate and chlorite. Cr-spinel alteration is more severe in the nodular chromitite than in the massive variety, presumably because of the relative sizes and surface areas of the pods and of the crystals therein and the differing availability of silicate phases for exchange (González-Jiménez et al., 2011).

4. Analytical methods

Spot chemical analyses, back-scattered electron images (BSE) and X-ray mapping were obtained from polished, carbon-coated thin-sections using a five-spectrometer JEOL JXA-8200 electron microprobe (EPMA) housed at the Division of Geological and Planetary Sciences (GPS), California Institute of Technology (Caltech), USA. Operating conditions were 15 kV accelerating voltage, 25nA beam current, a focused beam (1 μm) and 20 s on-peak counting times. A set of natural and synthetic mineral standards were used including synthetic forsterite, fayalite, Mn-olivine, anorthite, TiO_2, and Cr_2O_3; Amelia albite, Asbestos microcline, and Durango apatite. The mean atomic number background subtraction method and the CITZAF matrix correction routine were used. Calculations of structural formulae normalized to convenient formula units for each mineral used either custom Microsoft Excel spreadsheets or Minpet software (Richard, 1995).

The serpentine species were determined using Raman spectroscopy (Renishaw InVia micro-Raman spectrometer with 514 nm Ar-ion laser) at the GPS Division, Caltech. Phase identifications were verified using the reference spectra of Bahrambeygi et al. (2019) in both the 200–1100 cm^{-1} silicate vibration range and the 3550–3850 cm^{-1} OH-stretching region.

Based on the petrographic study, 18 representative samples of the massive serpentinite were analysed for major oxides, trace and rare-earth elements at the Activation Laboratories Ltd. (ActLabs, Canada) or at Caltech. At ActLabs, major oxides were measured using the method of lithium metaborate/tetraborate fusion ICP-AES (package code 4B). Trace and rare-earth elements were measured using the sensitive ICP-MS technique (package code 4B2) following lithium borate fusion and acid digestion. Detection limits for the major oxides lie between 0.01% and 0.001% whereas those for trace elements are all < 1 μg/g and for rare-earth elements < 0.005 μg/g. Loss on ignition (LOI) was determined by weight difference after ignition at ~ 1000 °C. Precision and accuracy were controlled by analysis of international reference materials and replicate analyses, 1% for major elements and 2–5% for trace elements. The analytical precision and detection limits of the analyses performed at ActLabs are listed on the website of the laboratory at http://www.actlabs.com/list.aspx?menu=64&app=226&cat1=549&tp=12&lk=no.

At Caltech, whole-rock composition of major and minor elements (Si, Ti, Al, Fe, Mg, Ca, Na, K, P, and Mn expressed as weight percent oxides; Rb, Ba, Sr, Nb, Zr, Hf, Y, Zn, Cu, Ni, Co, Cr, V, La, Ce, Nd, Pb, and Th expressed as elemental μg/g) were determined using a Panalytical Zetium XRF system. Sample powders were ground in an agate ball mill, loss on ignition (LOI) was determined by firing in air for 1 h at 1050 °C, and fused-glass beads were prepared from fired powders by mixing with 9 times their weight in 66.67% $Li_2B_4O_7$-32.83% $LiBO_2$-0.50% LiI flux and fusing at 1200 °C. After the XRF measurements, 25 ± 1 mg chips of the fused-glass beads are dissolved in acid-washed Teflon containers by refluxing in hot (250 °C) 3:1 nitric and hydrofluoric acid for at least 8 h. After dilution with milli-Q distilled water to 30 mL total volume, the rare-earth elements (REE) and some trace element concentrations (Cr, Cu, Ni, V, Co, Sc, Rb, Ba, Nb, Sr, Zr, Ta, Th, Pb, Zn, Cs, Mo, Hf, W and U) were determined using an Agilent Technologies 8800 triple quadrupole ICP-MS. A working curve for instrument sensitivity was developed using a blank fused bead from the same batch of flux used to prepare the unknowns along with the USGS standards AGV-2 and RGM-2. For quality control, additional USGS standards (DTS-2, BCR-1, G-2) were used as unknowns.

5. Mineral chemistry

5.1. Serpentinite

EMPA analysis of representative samples of massive serpentinite focused on serpentine, amphibole, clinopyroxene and Cr-spinel. Complete microprobe results are given in Supplementary Tables 1S to 4S.

Chemical analyses of serpentine minerals and their calculated structural are given in Supplementary Table 1S. Raman spectroscopy can be used to distinguish among the polytypes of serpentine. Silicate vibration peaks of antigorite appear at 230, 375, 683 and 1044 cm^{-1}; lizardite at 231, 384 and 1096 cm^{-1}; and chrysotile at 231, 389 and 1105 cm^{-1} (Fig. 5**a, b**); antigorite also displays a prominent doublet in the OH-vibration band at 3665 and 3700 cm^{-1}, whereas lizardite and chrysotile display singlet OH peaks. Raman spectra indicate that antigorite is the most abundant serpentine polytype, followed by minor

Table 1
Major element contents and normative composition of serpentinized peridotite of Hagar Dungash area.

Sample	R2	R11	R11†	R13	R15*	R21*,†	R22*	R30*	R34†	R65*	R67*	R68	R73	R74*	R76	R78*	R81	K15*,†
Major oxides (wt.%)																		
SiO_2	38.55	39.86	40.14	39.43	35.17	40.00	36.14	35.94	36.93	35.81	35.97	39.14	39.52	36.56	39.62	36.04	38.49	38.74
TiO_2	0.01	0.02	0.03	0.01	0.02	0.03	0.02	0.02	0.03	0.04	0.02	0.03	0.04	0.04	0.03	–	0.04	0.02
Al_2O_3	0.67	0.70	0.63	0.53	0.54	0.46	0.55	0.61	0.49	0.71	0.42	0.41	0.39	0.59	1.01	0.60	0.71	0.26
$Fe_2O_3^t$	7.47	7.33	7.10	8.04	6.51	8.28	7.72	7.65	8.54	6.74	7.52	7.87	8.96	6.74	7.23	6.65	6.48	7.14
MnO	0.06	0.11	0.09	0.06	0.08	0.07	0.08	0.08	0.12	0.07	0.13	0.12	0.07	0.10	0.13	0.05	0.06	0.19
MgO	38.19	37.48	38.07	37.92	41.53	36.44	42.55	43.03	37.77	41.13	43.32	38.05	38.86	43.26	37.68	41.11	38.40	38.66
CaO	0.99	0.71	0.69	0.91	2.17	0.10	0.74	0.79	0.57	1.74	0.38	0.79	0.31	0.61	0.33	1.68	1.51	0.35
Na_2O	0.01	0.01	0.01	0.01	0.01	0.00	0.02	0.02	0.00	0.03	0.01	–	0.01	0.02	0.01	0.02	0.01	0.00
K_2O	–	–	0.00	–	0.02	0.00	0.01	0.02	0.00	0.01	0.01	–	–	0.02	–	0.01	–	0.00
P_2O_5	0.02	0.03	0.02	0.03	0.03	0.01	0.01	0.01	0.01	0.02	0.01	0.03	0.02	0.02	0.04	0.02	0.02	0.01
LOI	13.54	13.84	13.49	13.01	14.23	11.13	11.84	12.02	14.12	13.64	11.74	12.71	11.36	12.34	13.68	14.05	14.27	12.38
Total	99.51	100.09	100.26	99.95	100.31	97.57	99.68	100.19	98.57	99.94	99.53	99.15	99.54	100.30	99.76	100.23	99.99	98.21
Mg#	0.910	0.910	0.914	0.903	0.927	0.897	0.916	0.918	0.898	0.924	0.919	0.905	0.896	0.927	0.912	0.925	0.922	0.91
Normative composition																		
Corundum	–	–	–	–	–	–	–	–	–	–	–	–	–	–	0.57	–	–	–
Orthoclase	–	–	–	–	–	0.07	0.07	0.14	–	–	0.07	–	–	0.14	–	0.07	–	–
Albite	0.10	0.10	0.10	0.10	–	0.19	0.19	0.19	–	–	0.10	–	0.10	0.19	0.10	0.20	0.10	–
Anorthite	2.09	2.18	1.94	1.62	1.57	1.73	1.58	1.73	1.60	2.01	1.23	1.30	1.17	1.67	1.61	1.77	2.22	1.45
Diopside	2.76	1.34	1.47	2.66	8.24	5.98	2.00	2.10	1.34	5.99	0.67	2.38	0.35	1.29	–	6.12	5.03	0.38
Hypersthene	24.33	33.52	33.08	28.49	–	0.32	2.70	0.09	21.34	–	2.58	28.37	28.62	4.10	34.86	1.88	21.27	9.06
Olivine	68.31	60.43	61.06	64.58	89.17	89.42	90.99	93.32	72.96	91.04	92.92	65.35	66.97	90.32	60.40	87.77	69.13	86.78
Magnetite	1.92	1.90	1.82	2.05	1.65	1.79	1.95	1.93	2.26	1.79	1.92	2.04	2.26	1.71	1.88	1.70	1.68	1.83
Ilmenite	0.02	0.04	0.07	0.02	0.04	–	0.04	0.04	0.07	0.09	0.04	0.07	0.09	0.09	0.07	–	0.09	0.04
Apatite	0.05	0.08	0.05	0.08	0.07	0.05	0.03	0.02	0.03	0.05	0.03	0.08	0.05	0.05	0.10	0.05	0.05	0.03
Colour Index	97.35	97.24	97.50	97.79	99.10	97.52	97.69	97.48	97.97	98.91	98.14	98.21	98.28	97.50	97.20	97.47	97.21	98.09
Diff. Index	0.10	0.10	0.10	0.10	–	0.26	0.26	0.33	–	–	0.16	–	0.10	0.33	0.10	0.27	0.10	–

* Serpentinite with dunite protolith.
† Samples analyzed at Caltech, USA; other samples analyzed at Actlabs, Canada.

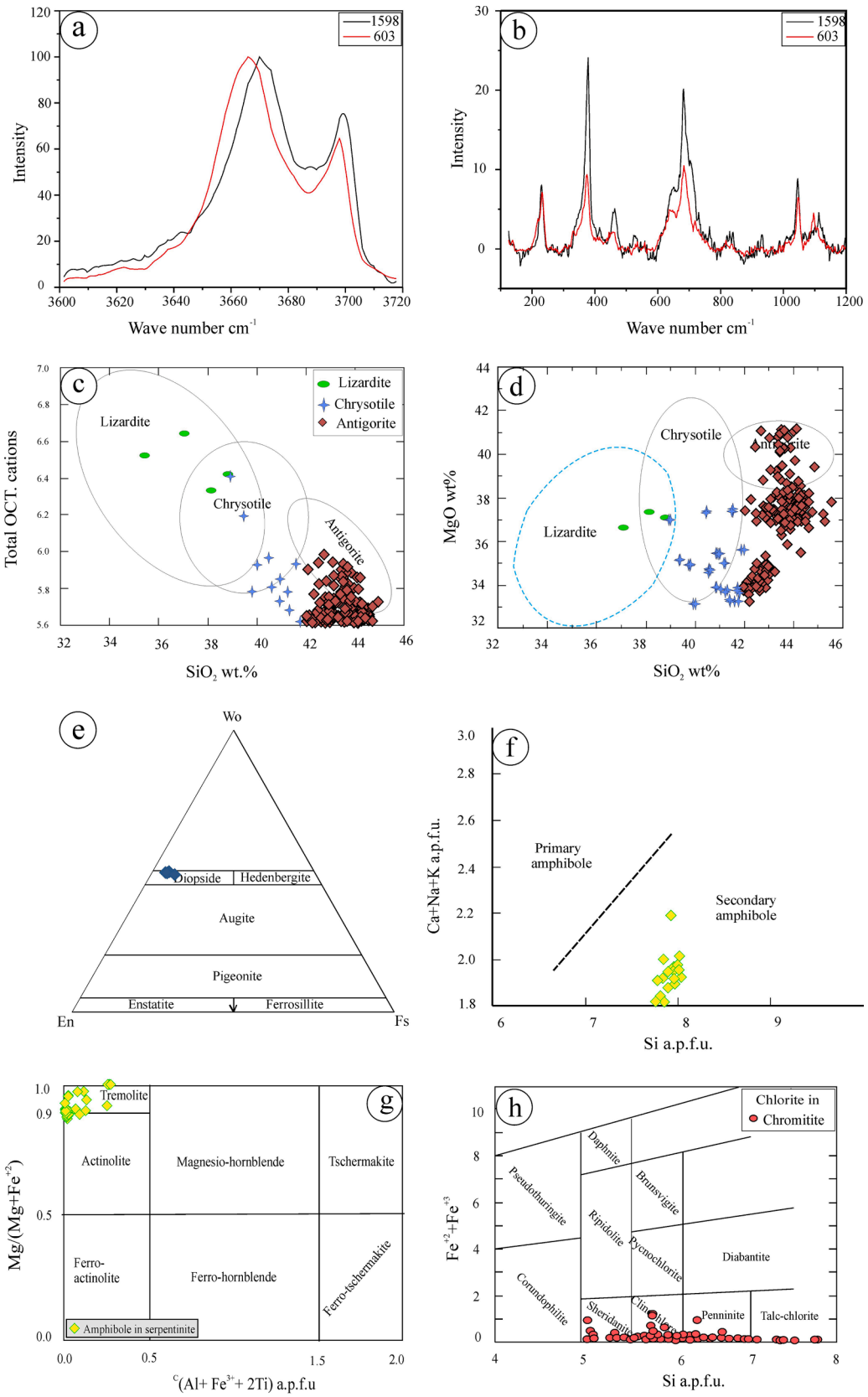

Fig. 5. Mineral chemistry plots: (a) OH-stretching region and (b) silicate band regions of the Raman spectra of serpentine minerals in the serpentinized peridotite, matching all peaks in the reference spectra for antigorite; (c) SiO_2 vs. total octahedral cations and (d) SiO_2 vs. MgO classifications diagrams for serpentine polymorphs (Bahrambeygi et al., 2019); (e) Pyroxene quadrilateral with nomenclature of Morimoto et al. (1988); (f) Discrimination diagram for primary and secondary amphiboles (Keeditse et al., 2016); (g) Classification diagram for calcic amphibole-group minerals (Hawthorne et al., 2012); (h) Classification diagram for chlorite-group minerals (Hey, 1954).

chrysotile and even more scarce lizardite. Chemically, antigorite contains more SiO_2 than lizardite or chrysotile (Whittaker and Wicks, 1970), corresponding to higher total octahedral occupancy in chrysotile and especially lizardite. MgO contents of the polytypes overlap, although antigorite often shows high and relatively homogeneous MgO (Dungan, 1979). The serpentine polytype discrimination diagrams of Bahrambeygi et al. (2019) indicate results similar to the Raman spectroscopy: most analyses are antigorite, with fewer chrysotile analyses and even fewer lizardite points **(**Fig. 5**c, d)**. Note that the fields defined by Bahrambeygi et al. (2019) in the MgO vs. SiO_2 diagram were developed from study of a locality with very low FeO in antigorite; the HD locality includes populations of significantly more FeO-rich antigorite, which therefore plot in the antigorite field defined by Bahrambeygi et al. (2019) in terms of total octahedral cations but below the field defined in terms of MgO only. The analyzed serpentine minerals exhibit variation in Mg# (molar Mg/[Mg + Fe]) both within and among samples; in sample R11 (whole-rock Mg# = 0.914), serpentine Mg# = 0.94 ± 0.03 (1σ) with a total range 0.82–0.98 (n = 145), whereas in sample R68 (whole-rock Mg# = 0.905), serpentine Mg# = 0.88 ± 0.01 with a range 0.87–0.89 except for one outlier at 0.83 (n = 43). Generally, in both samples, the antigorite is higher and more homogeneous in Mg# (though sample R11 contains a cluster of very high Mg# antigorite analyses), while the tails of the distribution to low Mg# are contained in chrysotile and especially lizardite.

The chemical analyses of relict pyroxene and calculated structural formulae are given in Supplementary Table 2S. Pyroxene relics large enough to measure were only found in one of the two massive serpentinite samples analyzed for mineral chemistry. The analyzed pyroxene is exclusively diopside **(**Fig. 5**e)** (Morimoto et al., 1988). Its composition is nearly homogeneous, with 25.4–25.7 wt% CaO, 55.3–55.8 wt% SiO_2, and very low alkalis (≤0.01 wt% K_2O and ≤ 0.04 wt% Na_2O), NiO (≤0.04 wt%), Cr_2O_3 (0.06–0.16 wt%), TiO_2 (<0.01 wt%) and Al_2O_3 (<0.02 wt%). Mg# is restricted to 0.93–0.94, which is characteristic of trace diopside in highly depleted residual mantle harzburgite protoliths (Jan and Windley, 1990; Arai, 1992), commonly found in fore-arc SSZ peridotites (e.g., Ishii et al., 1992). The very low Al_2O_3 contents in diopside support a depleted harzburgite protolith (Xiong et al., 2018).

Amphibole analyses and structural formulae are given in Supplementary Table 3S. The analyzed amphibole is exclusively secondary **(**Fig. 5**f)** calcic tremolite and actinolite based on the classification of Hawthorne et al. (2012) (Fig. 5**g**). The secondary origin of the analyzed amphibole is supported by its low TiO_2 (≤0.03 wt% and ≤ 0.003 Ti cations per formula unit) (Girardeau and Mevel, 1982).

Analyses of Cr-spinel from the serpentinite samples are given in supplementary table 4S. Although Cr-spinel in serpentinite is an accessory mineral, its textural and chemical characteristics are frequently the most diagnostic petrogenetic indicators in heavily altered ultramafic rocks. The massive serpentinite samples have Cr-spinel with distinct fresh cores, characteristically mantled by ferritchromite. The fresh Cr-spinel cores show high contents of Cr_2O_3 (54.3–57.3 wt%) and total iron as FeO^t (27.2–34.4 wt%); moderate MgO (2.1–4.3 wt%) and Al_2O_3 (7.1–10.4 wt%); low MnO (0.65–0.83 wt%); and extremely low TiO_2 (0.02–0.13 wt%). The Cr# (molar Cr/[Cr + Al]) ranges from 0.78 to 0.84 and Mg# varies between 0.12 and 0.23. Fresh Cr-spinel is characterized by very low Fe^{3+}# (molar $Fe^{3+}/[Fe^{3+}+Al+Cr] = 0.01–0.07$). Ferritchromite rims on zoned Cr-spinel crystals in serpentinite have high Cr# and Fe^{3+}# (0.88–0.98 and 0.10–0.23, respectively) and low Mg# (0.07–0.10).

5.2. Chromitites

Electron probe analyses of Cr-spinel, serpentine, chlorite and carbonates in the massive and nodular chromitite samples are given in Supplementary Tables 5S to 8S.

Cr-spinel in the massive chromitite is mostly fresh and characterized by variable, moderate to high Cr# (0.60–0.85), intermediate to high Mg# (0.51–0.82), low Al# (molar $Al/[Fe^{3+}+Al+Cr] = 0.15–0.41$), and extremely low Fe^{3+}# (≤0.05). Fresh Cr-spinel in nodular chromitite is notably different in chemistry. Cr# is uniformly very high (0.79–0.87), Mg# variable but systematically lower than in massive chromitite (0.27–0.57), Al# is low and more restricted in range (0.12–0.19), and Fe^{3+}# is higher (0.04–0.09). All these features are consistent with low-temperature exchange between Cr-spinel and silicate minerals having a larger effect on spinel chemistry in the nodular chromitite than in the massive chromitite, though there may have been differences in the primary Cr-spinel composition as well.

The interstitial serpentine minerals in chromitite are apparently quite variable in composition; this may reflect a very fine grain size and incorporation of other phases within the analytical volumes. One low-Si chrysotile point was observed (36.9 wt% SiO_2); the remaining antigorite points have 40.4–46.1 wt% SiO_2. Al_2O_3 (2.0–6.9 wt%) and Cr_2O_3 (1.2–7.1 wt%) are notably elevated. FeO^t is very low in most points (≤1.4 wt% except for one outlier at 3.7 wt%) and Mg# is very high (≥0.99 except for the outlier point at 0.94).

The interstitial chlorite has wide ranges of SiO_2 (26.0–37.8 wt%), MgO (29.0–37.5 wt%), Al_2O_3 (5.5–24.1 wt%) and FeO^t (0.28–5.5 wt%). The chlorite structure accommodates wide ranges of cation substitutions, particularly in the octahedral sites. Structurally, the numbers of Si cations in the chlorite formulae suggest sheridanite, clinochlore, penninite and talc-chlorite species according to the classification of Hey (1954), as shown in Fig. 5**h**. The optical properties and chemical composition of interstitial chlorite in the HD chromitites indicate elevated and abnormal concentrations of Cr_2O_3 (up to 15 wt%, Table 7S). According to Lapham (1958) and McCormick (1975), chromian chlorites can be sub-divided by the dominant structural location of Cr^{3+} into kämmererite (octahedral Cr^{3+}) and kotschubeite (tetrahedral Cr^{3+}) (neither of these varieties is an accepted mineral name). By this standard, chlorite in the HD chromitites is kämmererite; the Cr^{3+} must be dominantly octahedral because tetrahedral sites are fully occupied by Si and Al^{IV} (8 a.p.f.u., Table 7S). Chlorite likely formed after serpentine (based on petrographic texture), possibly in a second, later stage of alteration. Most probably, this took place at greenschist facies conditions or above (i.e., $T > 300$ °C) during fluid-mediated reaction of primary Cr-spinel and serpentine to ferritchromite and chromian chlorite (Kapsiotis et al., 2007; Merlini et al., 2009; Kapsiotis, 2014; Abdel-Karim and El-Shafei, 2018).

Electron probe (Supplementary Table 8S) data confirm the petrographic observation that carbonate in the massive chromitite is mostly dolomite whereas nodular chromitite contains mostly magnesite. The dolomite contains low MgO (19.4–20.0 wt%) and high CaO (32.0–32.4 wt%). Magnesite contains MgO in the range 43.1–47.5 wt%, with very low CaO (nil-0.06 wt%) and MnO (0.02–0.07 wt%) but considerable amounts of FeO^t (1.1–4.3 wt%) indicating a minor but not negligible siderite component in solid solution.

6. Whole-rock geochemistry

Whole-rock chemistry of the massive serpentinized peridotite samples is given in Tables 1 (major oxides and CIPW norms), 2 (trace elements), and 3 (REE). Loss on ignition (LOI) ranges from 11.13 to 14.27 wt%, consistent with the structural water content of serpentine minerals and minor volatile contributions from carbonates and other hydrous minerals. In the massive (not carbonated or sheared) serpentinite samples selected for whole-rock analysis, the role of carbonates is minor. This is based on the low modal abundance of carbonates observed in hand sample and thin section in these samples and the close agreement between LOI values and those expected for serpentine. The modal percentages of primary minerals cannot be determined easily in these severely serpentinized rocks. Hence, normative mineralogy of the anhydrous analyses (Table 1) was calculated using Minpet Software (Richard, 1995). Plotting the normative mineralogy in the classification diagram of Coleman (1977), the HD serpentinites plot in the harzburgite

Table 2
Trace element contents (μg/g) of serpentinized peridotite of Hagar Dungash area.

Sample	R2	R11	R11†	R13	R15*	R21*,†	R22*	R30*	R34†	R65*	R67*	R68	R73	R74*	R76	R78*	R81	K15†
Ag	0.03	0.04	–	0.03	0.02	–	0.04	0.04	–	0.05	0.03	0.04	0.02	0.02	0.02	0.04	–	–
As	9.98	12.14	–	11.42	4.14	–	8.24	35.40	–	9.92	11.17	3.11	7.08	10.46	5.84	6.05	5.84	–
Ba	5.00	4.00	8.88	4.00	3.00	11.56	2.00	4.00	11.37	2.00	3.00	5.00	6.00	2.00	4.00	2.00	6.00	14.36
Be	1.05	0.35	–	0.06	0.75	–	1.27	0.67	–	1.18	0.35	0.07	0.06	0.15	0.09	0.97	0.02	–
Bi	0.06	0.13	–	0.08	0.14	–	0.13	0.14	–	0.16	0.21	0.11	0.06	0.12	0.12	0.15	0.01	–
Co	105	107	144	115	117	114	104	108	146	99	109	134	128	122	90	103	112	127
Cr	2458	1748	3336	2373	2272	9035	2723	2965	3032	2745	2690	2156	2378	3006	3101	3266	2268	2510
Cs	0.23	0.12	–	0.09	0.18	–	0.33	0.45	–	0.71	0.63	0.04	0.09	0.58	0.21	0.30	–	–
Cu	6.67	6.46	–	8.33	5.73	25.97	6.03	6.07	–	5.89	7.55	11.80	13.62	6.25	2.11	5.81	10.10	–
Ga	0.89	1.13	–	1.22	0.87	–	1.03	1.25	–	1.23	1.31	1.22	1.86	1.27	1.08	1.05	0.50	–
Hf	0.08	0.08	0.08	0.06	0.06	0.03	0.08	0.09	0.02	0.15	0.08	0.07	0.12	0.12	0.06	0.07	0.11	0.03
Li	2.10	3.10	–	2.20	1.70	–	1.90	2.20	–	3.20	2.40	0.20	0.50	3.10	4.60	1.80	0.70	–
Nb	0.12	0.13	0.43	0.12	0.19	0.23	0.14	0.17	0.20	0.22	0.30	0.10	0.14	0.25	0.15	0.14	0.08	–
Ni	2300	2333	2896	2117	2088	2590	2738	2624	2704	2862	2970	1411	2788	2737	2108	2566	2431	2780
Pb	0.40	0.45	–	0.47	0.43	0.69	0.32	0.33	0.85	0.57	0.61	0.71	0.50	0.38	0.41	0.48	0.58	0.18
Rb	0.83	0.85	0.09	0.85	0.92	0.25	0.71	0.88	0.31	1.16	1.32	1.18	1.02	1.46	0.88	0.70	1.03	0.20
Sb	0.57	4.64	–	0.53	0.54	–	0.55	0.54	–	0.37	0.42	0.52	0.47	0.48	0.27	0.39	0.92	–
Sc	6.66	6.09	4.46	7.79	6.11	5.28	6.63	6.86	11.58	5.63	4.98	12.14	5.08	6.25	8.08	5.88	7.36	6.84
Se	0.20	0.30	–	0.30	0.30	–	0.30	0.30	–	0.30	0.04	0.30	0.20	0.20	–	0.30	0.20	–
Sn	0.66	0.17	–	0.10	0.48	–	0.78	1.42	–	1.19	1.08	0.12	0.14	1.64	0.11	0.84	0.02	–
Sr	14.15	11.26	5.88	11.98	8.35	5.47	5.50	5.57	27.49	5.96	7.23	16.59	14.55	6.34	9.65	6.90	13.20	14.16
Ta	0.02	0.01	0.02	0.02	0.01	0.01	0.01	0.01	0.00	0.02	0.01	–	–	–	0.02	0.01	0.02	0.01
Th	0.02	0.02	0.03	0.01	0.02	<0	0.02	0.02	<0	0.04	0.01	0.01	0.02	0.03	0.02	0.02	0.03	0.07
U	0.14	0.09	0.15	0.09	0.01	0.05	0.02	0.03	0.02	0.02	0.03	0.01	0.02	0.02	0.03	0.01	0.01	0.01
V	32.60	28.40	22.48	31.90	28.70	38.85	31.40	32.60	42.62	28.60	30.40	41.20	33.40	34.80	21.80	25.80	30.10	14.75
W	0.48	0.38	–	0.47	1.22	–	1.93	2.56	–	2.87	1.67	0.62	0.33	2.24	0.51	2.05	0.37	1.80
Y	0.75	0.47	0.86	0.48	0.28	0.35	0.76	0.33	0.03	0.61	0.41	0.68	0.32	0.35	0.44	0.14	0.23	0.11
Zn	43.10	40.40	–	50.40	38.40	–	47.00	50.80	–	51.20	48.60	54.30	65.40	50.30	38.30	44.80	41.60	–
Zr	2.10	2.60	4.51	2.10	2.60	2.80	1.80	2.00	1.90	2.20	2.30	1.90	2.40	1.80	1.70	2.40	1.70	1.31

* Serpentinite with dunite protolith.
† Samples analyzed at Caltech, USA; other samples analyzed at Actlabs, Canada.

Table 3
Rare earth element contents (μg/g) of serpentinized peridotite of Hagar Dungash area.

Sample	R2	R11	R11†	R13	R15*	R21*,†	R22*	R30*	R34†	R65*	R67*	R68	R73	R74*	R76	R78*	R81	K15†
La	0.344	0.085	0.090	0.026	0.131	0.495	0.221	0.136	0.339	0.250	0.277	0.204	0.238	0.237	0.207	0.014	0.200	0.376
Ce	0.742	0.195	0.179	0.065	0.283	2.123	0.506	0.299	2.075	0.591	0.477	0.477	0.552	0.543	0.521	0.036	0.557	2.665
Pr	0.103	0.024	0.025	0.010	0.043	0.113	0.065	0.041	0.071	0.078	0.063	0.062	0.068	0.072	0.071	0.006	0.073	0.067
Nd	0.391	0.103	0.103	0.052	0.192	0.470	0.288	0.150	0.175	0.316	0.261	0.253	0.273	0.293	0.302	0.030	0.296	0.194
Sm	0.070	0.030	0.027	0.022	0.085	0.094	0.057	0.034	0.027	0.066	0.071	0.058	0.056	0.063	0.053	0.012	0.070	0.038
Eu	0.020	0.015	0.014	0.012	0.022	0.018	0.015	0.010	0.003	0.021	0.036	0.019	0.021	0.022	0.027	0.007	0.017	0.006
Gd	0.073	0.052	0.054	0.035	0.069	0.084	0.108	0.037	0.013	0.074	0.108	0.073	0.066	0.074	0.061	0.018	0.082	0.017
Tb	0.011	0.008	0.009	0.006	0.011	0.015	0.019	0.006	0.003	0.011	0.016	0.011	0.010	0.011	0.009	0.003	0.013	0.001
Dy	0.075	0.056	0.061	0.040	0.065	0.080	0.121	0.038	0.029	0.069	0.112	0.073	0.061	0.076	0.064	0.019	0.084	0.016
Ho	0.018	0.014	0.015	0.009	0.018	0.021	0.028	0.009	0.005	0.015	0.024	0.017	0.014	0.018	0.014	0.004	0.020	0.003
Er	0.053	0.041	0.042	0.028	0.049	0.041	0.081	0.026	0.019	0.045	0.075	0.050	0.042	0.053	0.043	0.012	0.059	0.010
Tm	0.008	0.007	0.007	0.005	0.008	0.005	0.013	0.004	0.004	0.007	0.012	0.008	0.006	0.008	0.007	0.002	0.009	0.001
Yb	0.048	0.044	0.044	0.032	0.051	0.027	0.083	0.025	0.045	0.042	0.083	0.049	0.040	0.052	0.042	0.013	0.058	0.024
Lu	0.007	0.007	0.007	0.005	0.010	0.004	0.013	0.004	0.007	0.006	0.014	0.007	0.005	0.007	0.006	0.002	0.008	0.005
ΣREE	1.963	0.681	0.677	0.347	1.037	3.588	1.618	0.819	2.815	1.591	1.629	1.361	1.452	1.529	1.427	0.178	1.546	3.424
Eu/Eu*	0.85	1.16	1.12	1.32	0.88	0.61	0.58	0.86	0.43	0.92	1.25	0.89	1.05	0.98	1.45	1.45	0.68	0.72
$(La/Lu)_n$	5.10	1.26	1.29	0.54	1.36	13.85	1.76	3.53	5.41	4.32	2.05	3.02	4.94	3.51	3.58	0.73	2.59	7.10
$(La/Sm)_n$	3.07	1.77	2.04	0.74	0.96	3.30	2.42	2.50	7.98	2.37	2.44	2.20	2.65	2.35	2.44	0.73	1.78	6.22
$(Gd/Lu)_n$	1.29	0.92	0.93	0.87	0.85	2.79	1.03	1.14	0.25	1.52	0.95	1.29	1.63	1.31	1.26	1.11	1.27	0.38

* Serpentinite with Dunite protolith.
† Samples analyzed at Caltech, USA; other samples analyzed at Actlabs, Canada.

and dunite fields (Fig. 6**a**), consistent with the observations of mesh textures in all massive samples and bastite textures in some. On the Al_2O_3-MgO-CaO ternary diagram (Fig. 6**b**), which effectively plots normalized anhydrous compositions, the entire serpentinite sample set plots in the field of metamorphic peridotites associated with ophiolitic suites (Coleman, 1977); none resemble ultramafic cumulates.

The serpentinite analyses are dominated by MgO and SiO_2. Samples assigned to harzburgite protoliths vary in their normative olivine content from 60.4 to 73.0 wt%, with a complementary range from 21.3 to 34.9 wt% hypersthene. On the other hand, serpentinite samples assigned to dunite parentage have 86.8 to 93.3 wt% olivine component and ≤ 9.1 wt% hypersthene component. That is, there is a clear gap between the two groups, as opposed to a continuum in normative mineralogy or bulk composition. $Fe_2O_3^t$ varies from 6.5 to 9.0 wt%, with overlapping range in harzburgite and dunite protolith samples and no correlation with normative olivine. All the serpentinite samples are low in TiO_2 (≤0.04 wt%), Al_2O_3 (0.39–1.0 wt%), CaO (0.10–2.2 wt%), Na_2O (<0.03 wt%), K_2O (≤0.02 wt%), P_2O_5 (≤0.03 wt%) and MnO (0.06–0.14 wt%) with no evident correlations between the minor oxides and normative mineralogy. The low CaO content is consistent with the low observed clinopyroxene abundance and the absence of plagioclase (which is also consistent with the low Al_2O_3 content). The modestly elevated CaO content in some samples (up to 2.17%, without concomitant elevation in Al_2O_3) is probably hosted in carbonates, even though the dominant observed carbonate mineral in thin section is magnesite. The serpentinite samples have uniformly high Mg#, from 0.895 to 0.927. Harzburgite protolith samples have lower average Mg# (0.907) than dunite protolith samples (0.922). In general, the Mg# of all the serpentinite samples are in the range of modern oceanic peridotites, Mg# >0.89 (Bonatti and Michael, 1989).

The serpentinite samples display about one order of magnitude ranges in the concentrations of most trace elements (Table 2); surprisingly the most enriched and most depleted samples in many elements are both dunite-protolith samples. The primitive mantle-normalized (McDonough and Sun, 1995) trace element patterns are shown in Fig. 6**c**, with serpentinite samples distinguished into harzburgite and dunite protolith samples. They are depleted relative to primitive mantle in most trace elements (Ag, Ba, Be, Bi, Ga, Hf, Li, Nb, Rb, Se, Sn, Sr, Ta, Th, W, Y and Zr). However, they display high concentrations of compatible elements such as the first-row transition metals Cr, Ni, and Co, consistent with a depleted mantle protolith. The serpentinite samples are slightly enriched in other moderately compatible elements (V, Zn, Cu and Sc), depleted in high field-strength elements (Nb, Zr, Ti, Y and Hf), depleted in large-ion lithophile elements (Rb, K, Ba and Sr), and enriched (in some cases, extremely enriched) in fluid-mobile elements (Li, U, As, Sb, Pb and Cs).

Concentrations of REE in the HD serpentinite samples are given in Table 3 and plotted as chondrite-normalized (McDonough and Sun, 1995) patterns in Fig. 6**d**. As with other incompatible trace elements, the serpentinite data are depleted relative to chondritic values and span about one order of magnitude range for heavy REE (HREE) and nearly two orders of magnitude for light REE (LREE). The most enriched and most depleted samples are both dunite protolith samples; the chondrite-normalized total REE abundances of harzburgite protolith samples vary from 0.14 to 1.07, whereas the dunite protolith samples have total chondrite-normalized REE spanning 0.07 to 1.40. The shapes of the patterns are mostly almost flat in the middle to HREE, with a couple exceptions [$(Gd/Lu)_n$ = 0.85 to 2.74]. LREE may be either moderately enriched or depleted compared to HREE [$(La/Lu)_n$ = 0.53 to 13.5]. Samples exhibit a range of Eu anomalies from negative to positive [Eu/Eu* = 0.45–1.46].

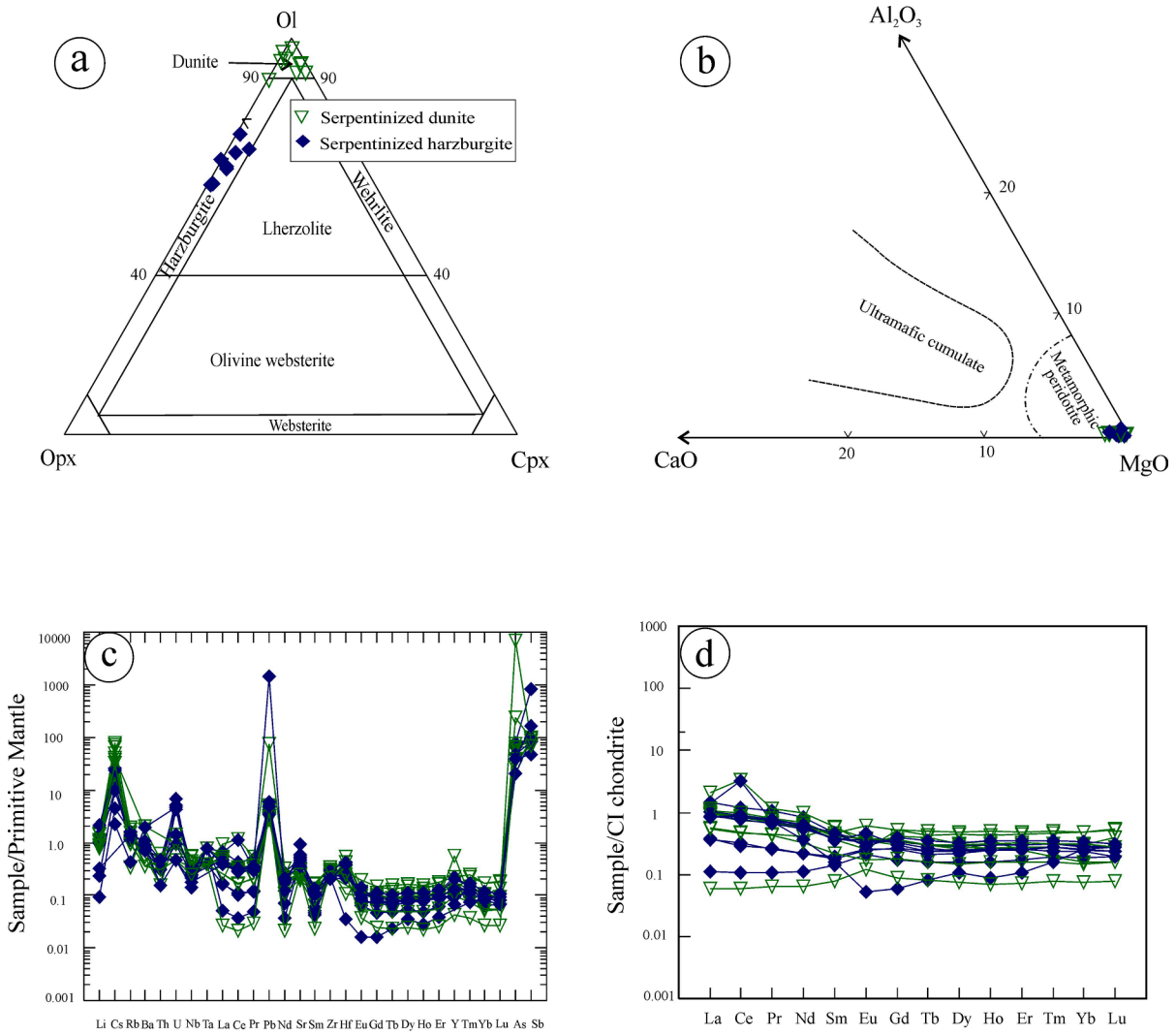

Fig. 6. Whole-rock chemistry plots for serpentinized peridotites: (a) ternary classification diagram for ultramafic rocks (Coleman, 1977); (b) Al_2O_3-MgO-CaO ternary diagram for separation of cumulate and residual peridotite (Coleman, 1977); (c) Primitive mantle-normalized trace elements patterns; (d) CI-chondrite normalized rare-earth element patterns (Primitive mantle and CI-chondrite normalization values of McDonough and Sun, 1995).

7. Discussion

7.1. The Hagar Dungash chromitite in a global context

Deeper understanding of the origins of ophiolite-hosted chromitite ores — including their tectonic setting and their multistage magmatic, metamorphic, and alteration histories — contributes to the twin goals of optimizing production of Cr and of constraining the evolution of seawater, of oceanic crust and of the underlying mantle through time (e.g., Dilek and Robinson, 2003). Ore bodies of podiform chromitite in the ophiolites of the world have ages ranging from Mesoarchaean (the ~ 3.5 Ga Selukwe Greenstone Belt, Zimbabwe) to Miocene (in New Caledonia) (Stowe, 1994). The Neoproterozoic ophiolites of the ANS occupy the middle of this temporal range, after the origin of modern-style plate tectonics but before the complete oxygenation of the deep ocean (e.g., Stolper and Bucholz, 2019). Therefore, the present study of the HD podiform chromitites and their host serpentinites offers insight into the prevailing conditions in the Neoproterozoic and into the accumulation of Cr^{3+} to form ores, especially in Precambrian shields similar to the ANS. In this context, it is potentially significant that the chromite reservoir in the mantle beneath the ANS appears to have been totally consumed by crystallization of chromite pods in the ophiolite. Most other podiform chromitite deposits in the world co-exist with stratiform chromite, whereas the mafic–ultramafic intrusions in the Eastern Desert of Egypt almost lack stratiform chromitite.

Recently, Arai (2021) suggested that podiform chromitites that remain at depth in the mantle differ essentially from those that end up becoming exposed at the surface in ophiolites. The possibility of such differences implies that studies of obducted chromitites form a necessary complement to study of *in situ* oceanic crust by international ocean drilling (e.g., Edwards et al., 2000). The melt-peridotite interactions modeled herein that lead to accumulation of Cr_2O_3 probably predate obduction and hence primary fresh chromitite pods that end up in ophiolites probably resemble those *in situ* beneath the oceans. However, the mobility of Cr during metamorphism to form non-retrograde Cr-chlorite (Khalil, 2007; Khedr and Arai, 2017; Azer et al., 2019) in the HD case and in similar SSZ ophiolites (e.g., Sepidbar et al., 2020) is likely a distinctive product of obduction and so study of this stage should illuminate the differences between ophiolite exposures and drilled samples.

In the following sections, we synthesize the petrographic, mineralogical and geochemical results for the mantle section of the Hagar Dungash ophiolite to clarify its petrogenesis and geotectonic setting. We then develop a quantitative model of the processes that may occur in such a setting and show how they may lead to a certain amount of monomineralic chromite precipitation with mineralogical characteristics matching the HD example.

7.2. Alteration and metamorphism

The ophiolitic ultramafic rocks of the HD area are highly altered and metamorphosed, with very limited preservation of original minerals, yet some primary textures are preserved. Metamorphism and subsequent alteration of the HD ultramafic rocks is expressed by serpentinization, carbonation and listvenitization. Serpentinization is the most dominant, penetrative alteration process, accompanied by more localized formation of listvenite, talc-carbonate rocks and magnesite veins along shear zones and fault planes. We find that the serpentinites are dominated by antigorite with subordinate lizardite and chrysotile. In general, serpentine minerals may form by hydration of primary ferromagnesian mantle minerals or by recrystallization of earlier serpentine phases (Deer et al., 1992). Antigorite is the most common prograde reaction product whereas lizardite is the most common retrograde reaction product. As chrysotile is found as cross-cutting veins truncating serpentine flakes, it appears that the protoliths of the HD area were mostly serpentinized during heating and burial (Moody, 1976; Deer et al., 1992), with minor retrograde formation of chrysotile and lizardite after antigorite. The dominance of antigorite over chrysotile and lizardite suggests peak metamorphic temperatures of 400–600 °C (Evans, 2010) during the main stage of serpentinization, implying also significant burial depth.

Disseminated primary Cr-spinel in serpentinite is altered to ferritchromite and Cr-magnetite along cracks and around the crystal boundaries. Ferritchromite is enriched in total iron and strongly depleted in Al_2O_3 and MgO, reflecting the loss in Al_2O_3 and Cr_2O_3 and increase in Fe_2O_3 during alteration. This is a fluid-mediated post-magmatic alteration process, usually attributed to the effects of metamorphism from low- to medium-grade greenschist facies up to lower amphibolite facies conditions (e.g., Thalhammer et al., 1990; McElduff and Stumpfl, 1991), consistent with the conditions of serpentinization to antigorite. Replacement of Cr-spinel by ferritchromite requires interaction with neighboring silicate phases as a source of Al and Fe and a sink for Mg; it operates to a very limited extent in massive chromitite, where exchange phases are scarce. The fresh Cr-spinels have very low Fe^{3+} contents indicating that the primary source was equilibrated at relatively low oxygen fugacity conditions (Murck and Campbell, 1986), while high Fe^{3+} in the ferritchromite and Cr-magnetite rims suggest an oxidative state during metamorphism (Anzil et al., 2012).

Chromian chlorite (kämmererite) is recorded as an interstitial mineral around Cr-spinels in the HD chromitite lenses. This mineral variety has been observed in a few other serpentinites in the Eastern Desert of Egypt (Azer and Stern, 2007; Gahlan et al., 2018). The presence of kämmererite may indicate replacement of Cr-spinel and serpentine during prograde regional metamorphism or later alteration. The significant Cr content of kämmererite and its petrographic relationship to the primary Cr-spinel suggest that Cr and Al are liberated from Cr-spinel during alteration to ferritchromite, whereas Si and Fe are derived from neighboring silicate minerals (Azer and Stern, 2007). The occurrence of kämmererite around primary relics of Cr-spinel reflects a lower-temperature episode of replacement of Cr-spinel below 300 °C (Gahlan et al., 2018).

The metamorphic grade indicated by the mineral assemblages in the serpentinized ultramafic rocks in the HD area ranges from greenschist facies (olivine–opx–chrysotile/antigorite–ferritchromite-magnetite) to lower amphibolite facies (olivine–opx–talc–tremolite–antigorite–ferri tchromite–magnetite). This is supported by plotting the Cr-spinel data from serpentinite and chromitite pods from this study and from Abu El Ela and Farahat (2010) on the triangular Cr-Fe^{3+}-Al diagram **(**Fig. 7**a).** Ferritchromite rims surrounding fresh Cr-spinel cores with sharp compositional gaps likely indicate upper greenschist to lower amphibolite facies metamorphism (Evans and Frost, 1975; Frost 1991; Suita and Strieder, 1996; Barnes and Roeder, 2001; Mellini et al., 2005; Arai et al., 2006; Farahat 2008).

7.3. Protolith and geodynamic setting of serpentinites

Several geodynamic models have been proposed for the generation of Egyptian ophiolites of the Eastern Desert, invoking a range of geodynamic settings (e.g., Azer and Stern, 2007; Abu-Alam and Hamdy, 2014; Gamal El Dien et al., 2016; Khedr and Arai, 2016; Ali et al., 2020a; Abdel-Karim et al., 2021b). Although early work assumed that the Egyptian ophiolites formed at mid-ocean ridges (e.g., Zimmer et al., 1995), today there is a general consensus that they formed in SSZ environments (e.g., El-Sayed et al., 1999; Ahmed et al., 2001; Farahat et al., 2004; Azer and Khalil, 2005; Azer and Stern, 2007; Khalil and Azer, 2007; Abd El-Rahman et al., 2009; Azer, 2014; Khalil et al., 2014; Gahlan et al., 2015; Gamal El Dien et al., 2016; Khedr and Arai, 2016; Obeid et al., 2016; Boskabadi et al., 2017; Gahlan et al., 2018; Azer et al., 2019; Abdel-Karim et al., 2021b; Ali et al., 2020a, b). However, within the overall SSZ system, there is still argument about the relative importance of fore-arc and back-arc basins. The chemistry of metavolcanic rocks in the Egyptian ophiolites, which is transitional between island arc and mid-ocean ridge affinities has motivated some researchers (e.g., El-Sayed et al., 1999; Farahat et al., 2004; Abd El-Rahman et al., 2009) to infer a back-arc setting. However, it can be difficult to assign tectonic settings on the basis whole-rock chemistry in metavolcanic rocks that have experienced extensive fractional crystallization, alteration and metamorphism. Fore-arc and back-arc lavas both reflect the influence of hydrous subduction components and have overlapping chemical ranges (Azer and Stern, 2007). Hence the mantle sections may offer more definitive evidence for assigning a tectonic setting for the Egyptian ophiolites.

Petrographic observations and whole-rock compositions establish with confidence, despite the highly altered and replaced state of the samples, that the protoliths of the serpentinized peridotites in the HD area include harzburgite and dunite. Their high Mg#, low Al_2O_3, low CaO, and scarcity of clinopyroxene indicate highly refractory mantle material that experienced high degrees of partial melt extraction (Bonatti and Michael, 1989; Hirose and Kawamoto, 1995; Parkinson and Pearce, 1998; Deschamps et al., 2013). These are common features of serpentinites in the ANS (Ali et al., 2020a, Abuamarah et al., 2020; Abdel-Karim et al., 2021b; Gahlan et al., 2020a, b). On the MgO/SiO_2 vs. Al_2O_3/SiO_2 diagram (Jagoutz et al., 1979; Hart and Zindler, 1986), the serpentinite samples interpreted to have harzburgite protoliths plot at low Al_2O_3/SiO_2, in the area of overlap between fore-arc peridotites and the most depleted end of the abyssal peridotite array **(**Fig. 7**b)**. Serpentinite samples with dunite protoliths plot above the terrestrial mantle array and melt extraction trend, requiring the action of another process to increase their olivine/orthopyroxene and MgO/SiO_2 ratios (Deschamps et al., 2013). The low Al_2O_3 contents of the HD serpentinite samples are also similar to fore-arc peridotites **(**Fig. 7**c)**; their CaO contents are more difficult to interpret due to the probable effects of carbonation.

In extremely serpentinized peridotites with no relict primary silicate minerals, Cr-spinel may be the most reliable available petrogenetic indicator (e.g., Dick and Bullen 1984; Arai 1992, 1994; Zhou et al. 1996; Barnes and Roeder 2001; Ohara et al., 2002; Arif and Jan 2006). Cr-spinel compositions are very sensitive to bulk rock composition as well as changes in pressure, temperature, and oxygen fugacity (Dick and Bullen, 1984; Barnes and Roeder, 2001; Arif and Jan 2006). There may be confounding post-magmatic effects of fluid interaction (Gamal El Dien et al., 2019), but there appears to be a clear boundary between fresh and altered spinels in the HD serpentinite samples. The high Cr# of fresh Cr-spinel requires either high degrees of partial melting or extensive melt–rock interaction (Parkinson and Pearce, 1998; Pearce et al., 2000). However, the low TiO_2 content of this spinel argues against a melt-rock interaction origin for the serpentinite, as this process tends to enrich spinel in TiO_2.

When pyroxene is preserved in a residual peridotite or serpentinite, it can offer additional petrogenetic clues (e.g., Dick and Natland, 1996;

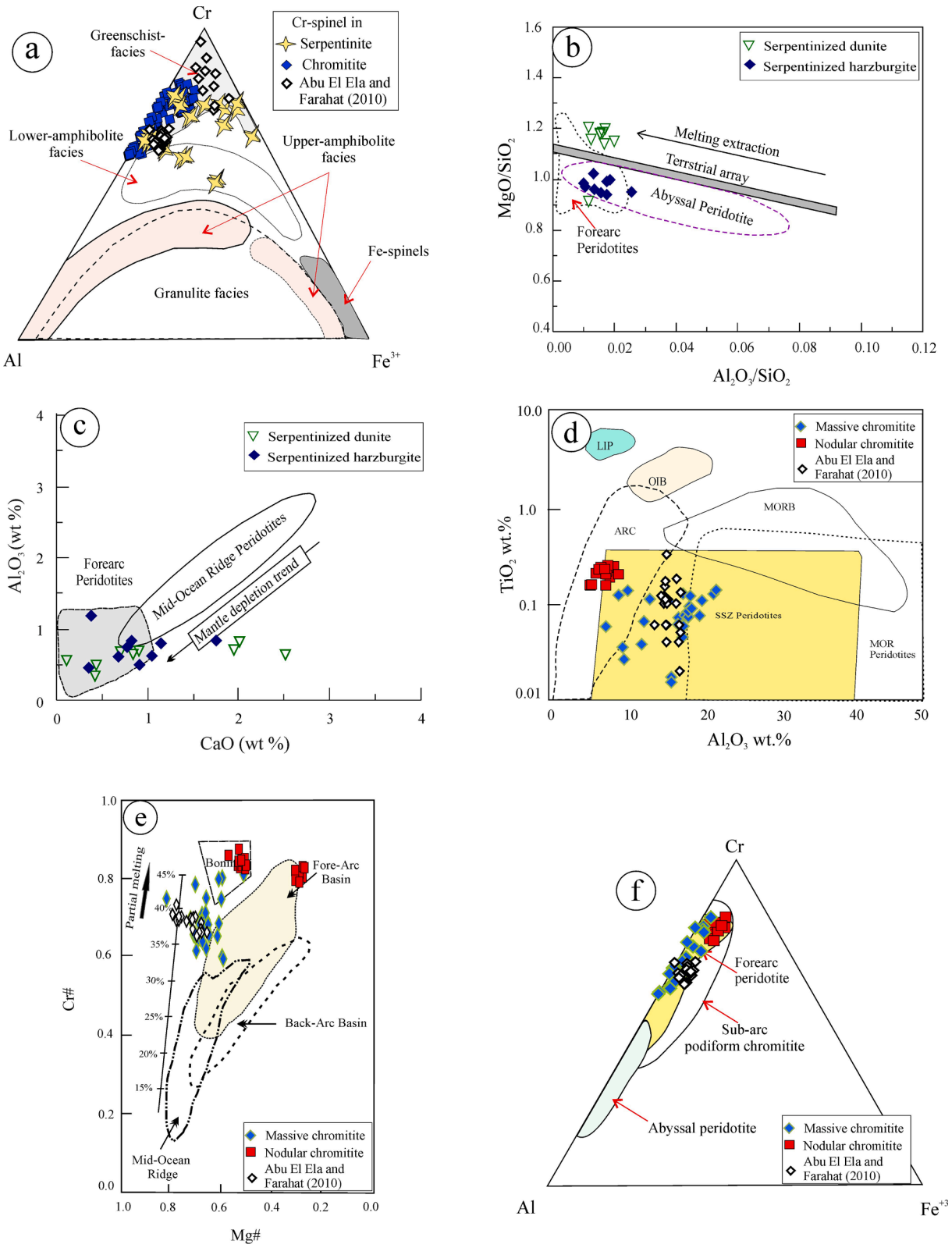

Fig. 7. Chemical discrimination diagrams to support the discussion of the HD ophiolite. (a) Evidence of metamorphic modification of Cr-spinel in serpentinite and lack thereof in Cr-spinel from chromitite; metamorphic fields on the triangular Cr-Fe^{3+}-Al^{3+} diagram are defined by Purvis et al. (1972), Evans and Frost (1975), and Suita and Strieder (1996); (b) Whole-rock MgO/SiO_2 vs. Al_2O_3/SiO_2 discrimination diagram for peridotites (Hart and Zindler,1986) showing current serpentinized harzburgite and dunite; (c) Whole-rock CaO vs. Al_2O_3 discrimination diagram for peridotites (Ishii et al., 1992), using anhydrous normalized oxide weight percents; (d) Al_2O_3 vs. TiO_2 in Cr-spinel from chromitite compared to tectonic fields of Kamenetsky et al. (2001); (e) Mg# vs. Cr# in Cr-spinel tectonic discrimination diagram after Stern et al. (2004) with field boundaries from Dick and Bullen (1984), Bloomer et al. (1995), and Ohara et al. (2002), and experimental melting trend from Hirose and Kawamoto, (1995); (f) Tectonic discrimination diagram based on trivalent cations (Cr- Al- Fe^{3+}) in Cr-spinel, applied to chromitite samples (Stern et al., 2004).

Pagé et al., 2008; Xiong et al., 2018). For example, Al content decreases and Mg# increases in residual mantle pyroxene with increasing degree of partial melting (e.g., Gasparik 1987; Dick and Natland, 1996). The low Al_2O_3 and high Mg# of fresh relics of clinopyroxene in the serpentinized peridotites from the HD area are consistent with those found in highly depleted fore-arc peridotites (e.g., Ishii et al., 1992; Pagé et al., 2008; Xiong et al., 2018). Similar compositions of fresh clinopyroxene have been recorded in serpentinized peridotites from other ANS ophiolites (e.g., Khalil et al., 2014; Obeid et al., 2016; Abuamarah et al., 2020; Abdel-Karim et al., 2021b; Ali et al., 2020a, b; Gahlan et al., 2020a).

The HD serpentinite samples **(**Fig. 6**c)** record significant to extreme enrichment in fluid-mobile elements (Li, Cs, Pb, U, As and Sb) relative to primitive mantle values. Such signatures have occasionally been assigned to inheritance from metasomatized or refertilized peridotite protoliths (Niu, 2004; Godard et al., 2008) but are more generally thought to reflect fluid percolation during serpentinization (Olivier and Boyet, 2006) at high fluid/rock ratios (Deschamps et al., 2012). Remarkably high contents of As and Pb may be hosted in serpentine (Deschamps et al., 2010) or in sulphides (Hattori et al., 2005); enrichment in these elements is a common feature of fore-arc serpentinites (Scambelluri et al., 2019). Seawater infiltration during serpentinization may be the source of relative enrichment in U (Deschamps et al., 2013), which may be hosted (along with Sr and Pb) in carbonates (Olivier and Boyet, 2006).

The REE patterns of the HD serpentinites are complex. They clearly do not express the extreme depletion of LREE relative to HREE expected (and observed) in residues of extensive melt extraction. Instead, they probably reflect modification by fluids or melts enriched in LREE, as might be found in a SSZ environment (Parkinson and Pearce, 1998; Zhou et al., 2005; Deschamps et al., 2013; Saka et al., 2014). Both positive and negative Eu anomalies are observed in the sample suite. The positive Eu anomalies might be attributed to interaction with Eu-enriched hydrothermal fluids during serpentinization (Paulick et al., 2006) but may also reflect preferential incorporation of Eu^{2+} in carbonate during carbonation (Boedo et al., 2015). On the other hand, negative Eu anomalies may reflect the local presence of talc in some serpentinite samples; this phase anomalously excludes Eu (Cárdenas-Párraga et al., 2017).

Many models have been suggested for the evolution of the Egyptian ophiolites; the range of models has recently converged around a growing consensus that these ophiolites formed in a fore-arc suprasubduction zone setting (Azer and Stern, 2007). The most recent model reflecting this setting was proposed by Abdel-Karim et al. (2021b). This model sets the several stages required to generate these ophiolites in the context of the opening and subsequent closing of the Mozambique Ocean between East and West Gondwana (Fig. 8). In the first stage, depleted peridotites were produced at a mid-ocean ridge (Fig. 8a). These depleted peridotites were subsequently drawn into a proto-fore-arc spreading center during subduction initiation (Fig. 8b). Finally, as the subduction zone matured towards a well-developed arc system, the new slab liberated a high flux of fluid (Fig. 8c) that drove high-degree partial melting of depleted peridotite. As we discuss in the next section, this scenario sets up a system in the final stage where hydrous basaltic melts may evolve into and mix with boninitic melts, yielding the observed assemblage of podiform chromitites embedded in serpentinites derived from dunite and harzburgite protoliths.

7.4. Origin of the chromitite pods

Turning to the Hagar Dungash chromitite pods in the present study, the Cr-spinel in the massive samples is generally homogenous and fresh, with only limited alteration to ferritchromite along cracks. The mineral and whole-rock chemistry of the serpentinite hosting the chromitite pods points to a fore-arc SSZ environment. Likewise, the high Cr# ($\geq$0.65) and low TiO_2 content ($\leq$0.2 wt%) of fresh Cr-spinel in the chromitite pods suggest crystallization from a high-Mg boninitic or tholeiitic magma, also associated with SSZ settings (Arai, 1994).

Using the Al_2O_3 vs. TiO_2 diagram of Kamenetsky et al. (2001), the Cr-spinel analyses from the massive HD chromitite pods from this study and from Abu El Ela and Farahat (2010) plot in the SSZ peridotite field **(**Fig. 7**d)**. The nodular chromitite pod analyses from this study form a distinct population, absent in the dataset of Abu El Ela and Farahat (2010). On the Cr# vs. Mg# discrimination diagram **(**Fig. 7**e)** (after Stern et al., 2004), Cr-spinel analyses from nodular chromitite divide into two groups. As noted above, Cr-spinel in nodular chromitite is more severely altered than that in massive chromitite; the altered spots form the population at low Mg# that coincidentally plots at the end of the field of fore-arc basin lava phenocrysts. On the other hand, the population of fresh analyses from the nodular chromitite pods (at higher Mg#) and some analyses from the massive chromitite pods plot in the field of phenocrysts from boninites **(**Fig. 7**e)**. Many of the new analyses from massive chromitite from this work, and all of the analyses from Abu El Ela and Farahat (2010), however, plot in a distinctive region at Cr# $\sim$ 0.65 and Mg# $\sim$ 0.7 that is not found as phenocrysts in any type of oceanic lava. This population may in fact fingerprint the distinctive process of mixing of boninitic and tholeiitic melt invoked in the model of podiform chromitite genesis; this will be considered in the quantitative model presented below. Note that the analyzed Cr-spinel from nodular chromitite sample plots at distinctively low Mg#; this is likely the result of protracted subsolidus Fe/Mg exchange with enclosing silicates. The experimentally calibrated partial melting trend for residual Cr-spinel indicates extents of melting $>$ 35 %, but it is unlikely that the chromitite pods are simple melting residues, so this result should be viewed with caution (Arai, 1994). On the Cr-Al-Fe^{3+} ternary diagram, although Cr-spinel from massive and nodular chromitite pods may be distinguished, both plot in the overlapping fields of fore-arc peridotites and SSZ podiform chromitite **(**Fig. 7**f)**.

7.5. A quantitative model for chromitite pod formation

Abuamarah et al. (2020) introduced a quantitative thermodynamic model for the origin of podiform chromitite by a multistage process of (1) melt extraction to yield depleted harzburgite, (2) melt-rock reaction driving the solid to dunite and the interstitial melt to boninite, and (3) mixing the boninite melt with unreacted tholeiitic melt to force supersaturation with Cr-spinel. The calculation uses the MELTS model (Ghiorso and Sack, 1995) and the methods of Asimow et al. (2001, 2004) and Asimow and Stolper (1999) to self-consistently compute the two end-member liquids and the liquidus relations of their mixtures. The original source composition is the "high-Na" depleted peridotite source of Workman and Hart (2005) with 150 μg g^{-1} H_2O; near-fractional melting was computed along an isentropic path that encountered its "damp" solidus at 3.3 GPa. The integrated melt produced by the system at 1 GPa is a primitive, low-SiO_2 tholeiitic basalt (with 46.5 wt% SiO_2, 11.3 wt% MgO, 0.018 wt% Cr_2O_3, and 0.38 wt% H_2O); this liquid constitutes the "unreacted" melt that is assumed to ascend without reaction through dunite conduits until it encounters the mixing region at lower pressure. The decompression melting and isentropic cooling continues to 0.1 GPa and 1310 °C, where the residue is a harzburgite with 73 wt% olivine, 25 wt% orthopyroxene, and 2 wt% Cr-spinel. This residue is reacted with a sufficient mass of the tholeiitic melt to exhaust orthopyroxene, yielding a dunite in equilibrium with a boninitic liquid (55.4 wt% SiO_2, 13.7 wt% MgO, 0.37 wt% Cr_2O_3, 1.42 wt% H_2O). Finally, these two liquids were mixed at 0.1 GPa pressure; for the two end-members and each intermediate mixture, the liquidus phase and the mass of Cr-spinel formed as a function of temperature below the liquidus were computed. The critical result presented in Abuamarah et al. (2020) is that, although both end-member liquids have olivine on the liquidus, mixtures with between 51 and 55 wt% SiO_2 have Cr-spinel on the liquidus. At the optimum mixture, with 53 wt% SiO_2, Cr-spinel crystallization begins about 4 °C before olivine crystallization, and a maximum

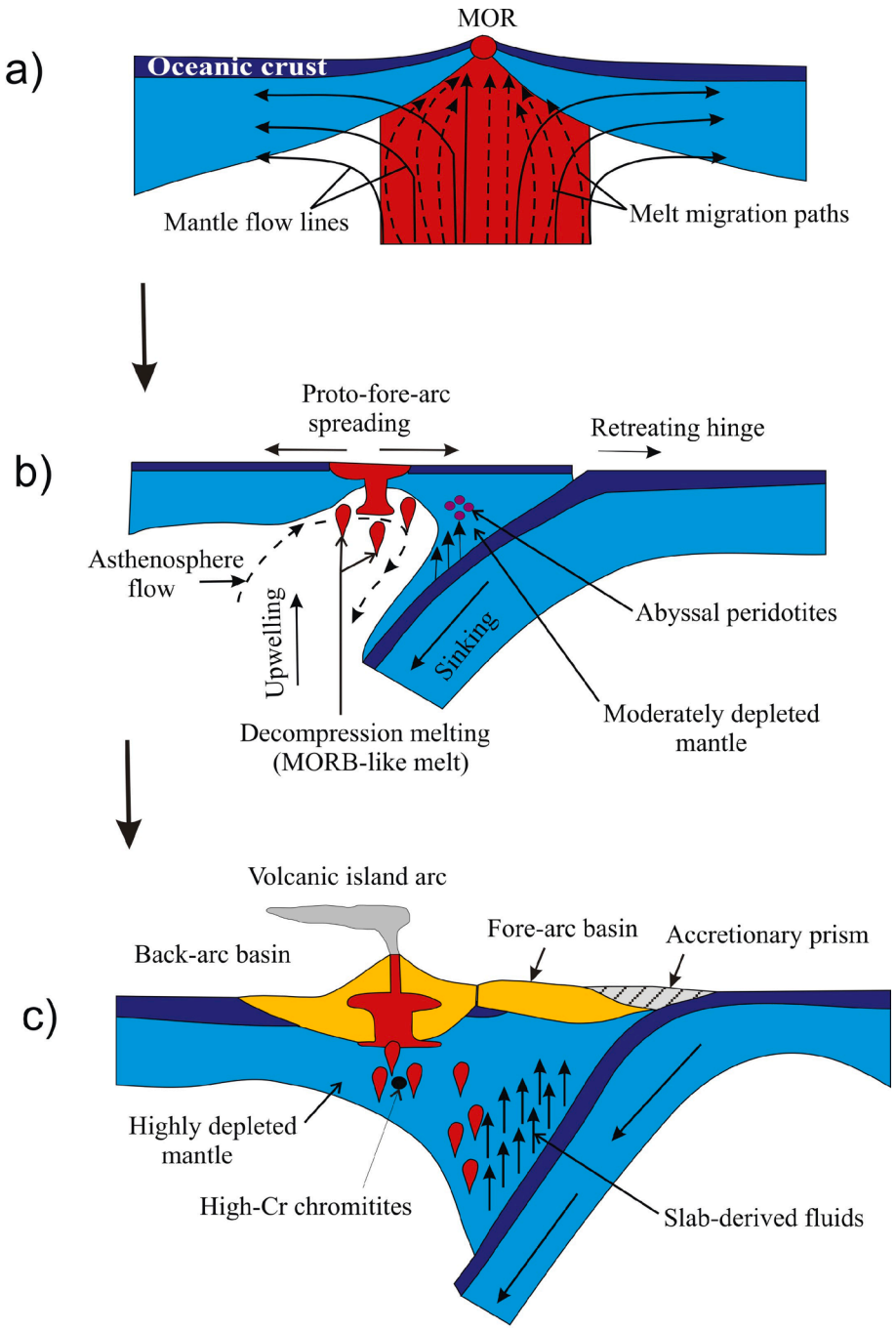

Fig. 8. Schematic illustration showing (a) opening of Mozambique Ocean between East and West Gondwana with development of depleted peridotite residual to mid-ocean ridge melt extraction; (b) subduction initiation or incipient arc stage, in which partial melting occurred in the mantle wedge and proto-fore-arc spreading started to form over the subduction zone; (c) the true subduction or mature-arc stage, associated with high fluxes of slab-derived fluids and high-degree partial melting of depleted mantle, producing hydrous melts that evolve to and mix with boninitic melts, from which the high-Cr chromitites were precipitated (Abdel-Karim et al. 2021b).

mass fraction of 1 g of Cr-spinel can be precipitated from 8.3 kg of mixed melt before olivine crystallization begins.

Here we extend the application of this model by showing its predictions for spinel mineral chemistry and comparing these to the Hagar Dungash peridotite and chromitite samples. Fig. 8 illustrates the systematics of Cr-spinel compositional variation in the MELTS model described in the previous paragraph. The boninite liquid that results from melt/peridotite reaction at low pressure has olivine on the liquidus, but when Cr-spinel begins crystallizing it has high Cr# ($\geq$0.7) and moderate Mg# ($\sim$0.75). With continued cooling and olivine + Cr-spinel fractionation, the Cr-spinel composition evolves down and to the right, towards lower Cr# and lower Mg#. The primary basalt composition that ascends without reaction in the dunite conduits also has olivine on the liquidus, and in this case when Cr-spinel begins crystallizing it has low Cr# ($<$0.6) and high Mg# ($\sim$0.79). With continued cooling, Cr-spinel composition again evolves (more steeply) down and to the right, towards lower Cr# and higher Mg# as long as the fractionating assemblage is olivine + Cr-spinel. When orthopyroxene joins the assemblage, the Cr-spinel evolution path kinks and moves rapidly down in Cr#. Subsequently, when clinopyroxene joins the assemblage, the Cr-spinel evolution path changes direction again and moves out into the field of observed Cr-spinels in fore-arc lavas along a path of increasing Cr# and decreasing Mg#. Most notably for the current study, the region of mixing between the boninite and primary basalt where Cr-spinel is on the liquidus and monomineralic chromitite pods may be precipitated occupies a region of the diagram at lower Cr# and higher Mg# than the boninite field, and at higher Cr# and higher Mg# than the evolved fore-arc basalt field. This is precisely the area of enigmatic Cr-spinel compositions found in the Hagar Dungash massive serpentinites (Fig. 7e).

Although the absolute Cr# of the MELTS model Cr-spinels are shifted

towards lower values than the Hagar Dungash data, there are often systematic errors in MELTS results when interrogated in detail. However, trends within the self-consistent model space due to changes in intensive variables and along petrologic process paths are often robust. Hence, we view the behavior of Cr-spinel chemistry in this model as a successful explanation for the presence of Cr-spinel in the massive chromitites with anomalous compositions. It appears to be a natural outgrowth of the melt/rock reaction and mixing scenario for the formation of podiform chromitite (see Fig. 9).

The ability of the MELTS-based model to match the trends in mineral composition within the HD chromitite pods lends additional confidence to the use of this model to understand the origin of such pods in general. The most essential prediction of the model is the relatively low efficiency of chromitite production, 1 g of chromite per 8.3 kg of melt that flows through the system. In fact, this low efficiency should not be surprising. The Cr_2O_3 content of the upper mantle is about 0.5 wt% (e.g., Workman and Hart, 2005) and oceanic crust is the product of approximately 10% partial melting. If a scenario could be found, hypothetically, in which Cr were perfectly incompatible during partial melting (and so quantitatively extracted from the mantle) and then became perfectly compatible during chromitite pod formation (and so all deposited in chromitite), the maximum imaginable efficiency would be 1 g of chromite per 20 g of melt. But such a case cannot be realized; Cr is in fact compatible during mantle melting, and primitive melts rarely carry more than ~ 0.05 wt% Cr_2O_3. Complete capture of all this Cr would yield 1 g of chromitite per 2 kg of melt. But Cr does not become perfectly compatible during chromitite genesis; by the time olivine returns to the liquidus after mixing, only a fraction (apparently, about 25%) of the Cr carried by the melt can be deposited in monomineralic chromite. Because a given section of oceanic upper mantle only experiences a certain melt flux before migrating away from a spreading center, a limit on chromite production per unit melt flux corresponds to a limit on the size of chromitite deposits that mid-ocean ridge type ophiolites can host. Increasing the size of such chromitite deposits requires highly focused melt flux, maintained over time in a given place, which may occur in settings where especially large fluxes of fluid are liberated from a downgoing slab during subduction initiation (e.g., Leng et al, 2012).

8. Conclusions

- The Hagar Dungash (HD) ophiolitic sequence — despite dismemberment, deformation, metamorphosis to lower amphibolite facies, and alteration — can be recognized as a supra-subduction zone fore-arc ophiolite dominated by serpentinite masses developed from highly depleted residual peridotites, enclosing lenses of chromitite.
- The podiform chromitite lenses include massive and nodular varieties. Massive chromitite is mostly fresh and composed mainly of Cr-spinel (>90 vol%) with minor interstitial minerals. Cr-chlorite (kämmererite) is observed among the interstitial minerals and as inclusions within the Cr-spinel crystals.
- The massive chromitite pods preserve magmatic compositions that enable comparison of their mineral chemistry to quantitative models of chromitite genesis. They contain a population of Cr-spinel cores with moderate Cr# (~0.70), high Mg# (>70), and very low TiO_2 content that differ from compositions found in any category of erupted lava. A model of mixing between boninitic melt formed by melt/peridotite reaction with unreacted primary fore-arc basalt ascending in dunite conduits can precipitate about 1 g of monomineralic Cr-spinel per 8.3 kg of melt flux, with chemical characteristics resembling those observed in the Hagar Dungash chromitite pods.

Credit authorship contribution statement

Hilmy E. Moussa: Investigation. **Heba S. Mubarak:** Investigation.

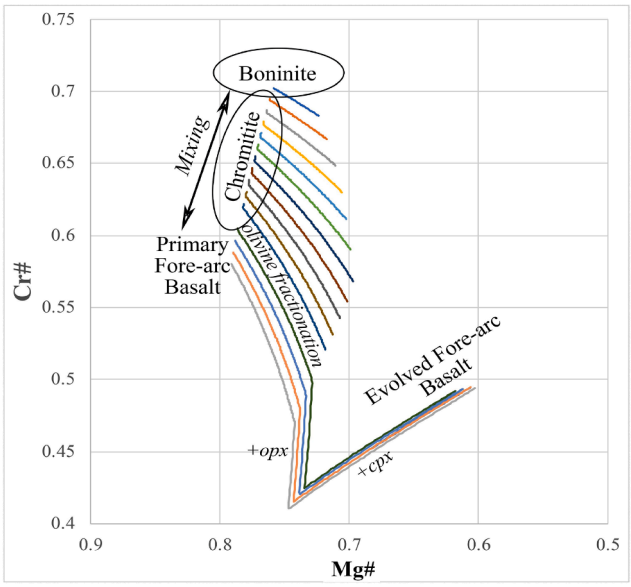

Fig. 9. Systematics of Cr-spinel chemical variation in the MELTS model of mixing between boninite and primary fore-arc basalt, followed by fractional crystallization, viewed in Cr# vs. Mg# space. The colored paths show successive Cr-spinel compositions crystallized during isobaric cooling at 0.1 GPa; the trends due to olivine + Cr-spinel fractionation, olivine + opx + Cr-spinel fractionation, and opx + cpx + Cr-spinel fractionation are marked. The near-liquidus region where monomineralic chromitite may precipitate from mixed melts is labelled "Chromitite". The mixing process leads to precipitation of Cr-spinel compositions with lower Cr# and higher Mg# than the boninite field, consistent with a large population of compositions measured in the HD massive chromitite pods.

Mokhles K. Azer: Conceptualization, Investigation, Visualization, Writing – original draft. **Adel A. Surour:** . **Paul D. Asimow:** Investigation, Methodology, Resources, Software, Validation, Writing – original draft. **Mona M.L. Kabesh:** .

Declaration of Competing Interest

The authors declare that they have no known competing financial interests or personal relationships that could have appeared to influence the work reported in this paper.

Acknowledgements

We acknowledge the National Research Centre (NRC), Egypt for logistical support of this work. The present manuscript is a part of the master's thesis of Heba S. Mubarak (the second author). PDA is supported by the United States NSF, award 1947616. We are grateful to the editor, Victoria Pease, and to five anonymous reviewers for their dedicated work in helping to improve the manuscript.

Appendix A. Supplementary data

Supplementary data to this article can be found online at https://doi.org/10.1016/j.precamres.2021.106507.

References

Abdel-Karim, A.A., El-Shafei, S.A., 2018. Mineralogy and chemical aspects of some ophiolitic metaultramafics, central Eastern Desert, Egypt: Evidence from chromites, sulphides and gangues. Geol. J. 53 (2), 580–599.

Abdel-Karim, A.M., El-Shafei, S.A., Azer, M.K., 2021a. Petrology and geochemistry of ophiolitic metaperidotites from the Eastern Desert of Egypt: Insights into geodynamic evolution and post-melting alteration processes. Acta Geol. Sin. 95 (4), 1139–1157.

Abdel-Karim, A., El-Shafei, S., Azer, M., 2021b. The Neoproterozoic ophiolitic ultramafic rocks in Eastern Desert of Egypt: implications for petrogenesis and metasomatic processes. Int. Geol. Rev. 63 (2), 208–232.
Abd El-Rahman, Y., Polat, A., Dilek, Y., Fryer, B., El-Sharkawy, M., Sakran, S., 2009. Geochemistry and tectonic evolution of the Neoproterozoic Wadi Ghadir ophiolite, Eastern Desert. Egypt. Lithos 113 (1–2), 158–178.
Abu El Ela, F.F., Farahat, E.S., 2010. Neoproterozoic podiform chromitites in serpentinites of the Abu Meriewa-Hagar Dungash district, Eastern Desert, Egypt: Geotectonic implications and metamorphism. Isl. Arc 19 (1), 151–164.
Ahmed, A., Arai, S., Attia, A., 2001. Petrological characteristics of the Pan African podiform chromitites and associated peridotites of the Proterozoic ophiolite complexes. Egypt. Mineralium Deposita 36, 72–84.
Ahmed, A.H., 2013. Highly depleted harzburgite–dunite–chromitite complexes from the Neoproterozoic ophiolite, south Eastern Desert, Egypt: A possible recycled upper mantle lithosphere. Precambr. Res. 233, 173–192.
Abuamarah, B.A., 2019. Geochemistry and fore-arc evolution of upper mantle peridotites in the Cryogenian Bir Umq ophiolite, Arabian Shield, Saudi Arabia. Int. Geol. Rev. 62 (5), 630–648.
Abuamarah, B., Asimow, P.D., Azer, M., Ghrefat, H., 2020. Suprasubduction-zone origin of the podiform chromitites of the Bir Tuluhah ophiolite, Saudi Arabia, during Neoproterozoic assembly of the Arabian Shield. Lithos 360, 105439.
Abu-Alam, T.S., Hamdy, M.M., 2014. Thermodynamic modeling of Sol Hamed serpentinite, South Eastern Desert of Egypt: Implication for fluid interaction in the Arabian-Nubian Shield ophiolites. J. African Earth Sci. 68, 1–14.
Ali, R.A.M., Pitcairn, I.K., Maurice, A.E., Azer, M.K., Bakhit, B.R., Shahien, M.G., 2020a. Petrology and geochemistry of ophiolitic ultramafic rocks and chromitites across the Eastern Desert of Egypt: Insights into the composition and nature of a Neoproterozoic mantle and implication for the evolution of SSZ system. Precambr. Res. 337, 105565.
Ali, R.A.M., Maurice, A.E., Pitcairn, I.K., Ahmed, A.H., Azer, M.K., Boskabadi, A., Bakhit, B.R., Shahien, M.G., 2020b. Neoproterozoic and Cretaceous mantle oxidation states: Controls and heterogeneity through time. Lithos 356–357, 105375.
Anzil, P., Guereschi, A., Martino, R., 2012. Mineral chemistry and geothermometry using relict primary minerals in the La Cocha ultramafic body: A slice of the upper mantle in the Sierra Chica of Córdoba, Sierras Pampeanas, Argentina. J. S. Am. Earth Sci. 40, 38–52.
Arai, S., 1992. Chemistry of chromian spinel in volcanic rocks as a potential guide to magma chemistry. Mineral. Mag. 56, 173–184.
Arai, S., 1994. Characterization of spinel peridotites by olivine-spinel compositional relationships: review and interpretation. Chem. Geol. 13, 191–204.
Arai, S., Yurimoto, H., 1994. Podiform chromitites of the Tari-Misaka ultramafic complex, southwestern Japan, as mantle–melt interaction products. Econ. Geol. 89, 1279–1288.
Arai, S., 1997. Control of wall-rock composition on the formation of podiform chromitites as a result of magma/peridotite interaction. Resour. Geol. 47, 177–187.
Arai, S., Abe, N., 1995. Reaction of orthopyroxene in peridotite xenoliths with alkali basalt melt and its implication for genesis of alpine-type chromitite. Am. Mineral. 80, 1041–1047.
Arai, S., 2021. Genetic link between podiform chromitites in the mantle and stratiform chromitites in the crust: A hypothesis. Minerals 11 (2), 209.
Arai, S., Matsukage, K., 1998. Petrology of a chromitite micropod from Hess Deep, equatorial Pacific: a comparison between abyssal and alpine-type podiform chromitites. Lithos 43, 1–14.
Arai, S., Shimizu, Y., Ismail, S., Ahmed, A., 2006. Low-T formation of high-Cr spinel with apparently primary chemical characteristics within podiform chromitite from Rayat, northeastern Iraq. Mineral. Mag. 70, 499–508.
Arai, S., Miura, M., 2016. Formation and modification of chromitites in the mantle. Lithos 264, 277–295.
Arif, M., Jan, M.Q., 2006. Petrotectonic significance of the chemistry of chromite in the ultramafic-mafic complexes of Pakistan. J. Asian Earth Sci. 27, 628–646.
Asimow, P.D., Stolper, E.M., 1999. Steady-state mantle-melt interactions in one dimension: I. equilibrium transport and melt focusing. J. Petrol. 40 (3), 475–494.
Asimow, P.D., Hirschmann, M.M., Stolper, E.M., 2001. Calculation of peridotite partial melting from thermodynamic models of minerals and melts. IV. adiabatic decompression and the composition and mean properties of mid-ocean ridge basalts. J. Petrol. 42 (5), 963–998.
Asimow, P.D., Dixon, J.E., Langmuir, C.H., 2004. A hydrous melting and fractionation model for mid-ocean ridge basalts: application to the mid-Atlantic ridge near the Azores. Geochem. Geophys. Geosyst. 5 (1), Q01E16.
Azer, M.K., Khalil, A.E.S., 2005. Petrological and mineralogical studies of Pan-African serpentinites at Bir Al-Edeid area, Central Eastern Desert, Egypt. J. African Earth Sci. 43, 525–536.
Azer, M.K., 2013. Evolution and economic significance of listvenites associated with Neoproterozoic ophiolites in south Eastern Desert. Egypt. Geologica Acta 11 (1), 113–128.
Azer, M.K., 2014. Petrological studies of Neoproterozoic serpentinized ultramafics of the Nubian Shield: Spinel compositions as evidence of the tectonic evolution of the Egyptian ophiolites. Acta Geol. Pol. 64, 113–127.
Azer, M.K., Gahlan, H.A., Asimow, P.D., Mubarak, H.S., Al-Kahtany, K.M., 2019. Multiple stages of carbonation and element redistribution during formation of ultramafic-hosted magnesite in Neoproterozoic ophiolites of the Arabian-Nubian Shield, Egypt. J. Geol. 127 (1), 81–107.
Azer, M.K., Stern, R.J., 2007. Neoproterozoic (835–720 Ma) serpentinites in the Eastern Desert, Egypt: Fragments of fore-arc mantle. J. Geol. 115, 457–472.
Bach, W., Garrido, C.J., Paulick, H., Harvey, J., Rosner, M., 2004. Seawater-peridotite interactions: First insights from ODP Leg 209, MAR 15°N. Geochem. Geophys. Geosyst. 5 (9), Q09F26.
Bahrambeygi, B., Moeinzadeh, H., Alavipanah, S., 2019. Mineralogy, Geochemistry and Raman Spectroscopy of Multi-Genesis Serpentine Polymorphs of Darepahn Ophiolites. J. Sci., Islamic Republic of Iran 30 (3), 251–269.
Barnes, S.J., Roeder, P.L., 2001. The range of spinel compositions in terrestrial mafic and ultramafic rocks. J. Petrol. 42, 2279–2302.
Bloomer, S., Taylor, B., MacLeod, C., Stern, R., Fryer, P., Hawkins, J., Johnson, L., 1995. Early arc volcanism and ophiolite problem: a perspective from drilling in the Western Pacific. In: Taylor, B., Natland, J. (Eds.), Active margins and marginal basins of the Western Pacific, geophysical monograph, DC 88. American Geophysical Union, Washington, pp. 1–30.
Boedo, F.L., Escayela, M.P., Pérez Luján, S.B., Vujovich, G., Ariza, J.P., Naipauer, M., 2015. Geochemistry of Precordillera serpentinites, Western Argentina: evidence for multistage hydrothermal alteration and tectonic implications for the Neoproterozoic-early Paleozoic. Geologica Acta 13 (4), 263–278.
Bonatti, E., Michael, P.J., 1989. Mantle peridotites from continental rifts to oceanic basins to subduction zones. Earth Planet. Sci. Lett. 91, 297–311.
Boskabadi, A., Pitcairn, I.K., Broman, C., Boyce, A., Teagle, D.A.H., Cooper, M.J., Azer, M.K., Stern, R.J., Mohamed, F.H., Majka, J., 2017. Carbonate alteration of ophiolitic rocks in the Arabian-Nubian Shield of Egypt: sources and compositions of the carbonating fluid and implications for the formation of Au deposits. Int. Geol. Rev. 59 (4), 391–419.
Cárdenas-Párraga, J., García-Casco, A., Proenza, J.A., Harlow, G.E., Blanco-Quintero, I. F., Lázaro, C., Villanova-de-Benavent, C., Núñez Cambra, K., 2017. Trace-element geochemistry of transform-fault serpentinite in high-pressure subduction mélanges (eastern Cuba): Implications for subduction initiation. Int. Geol. Rev. 59 (16), 2041–2064.
Coleman, R.G., 1977. Ophiolites. Springer-Verlag, Berlin Heidelberg New York, p. 229p.
Deschamps, F., Guillot, S., Godard, M., Chauvel, C., Andreani, M., Hattori, K., 2010. In situ characterization of serpentinites from forearc mantle wedges: timing of serpentinization and behavior of fluid-mobile elements in subduction zones. Chem. Geol. 269, 262–277.
Deschamps, F., Godard, M., Guillot, S., Chauvel, C., Andreani, M., Hattori, K., Wunder, B., France, I., 2012. Behavior of fluid-mobile elements in serpentinites from abyssal to subduction environments: examples from Cuba and Dominican Republic. Chem. Geol. 312–313, 93–117.
Deschamps, F., Godard, M., Guillot, S., Hattori, K., 2013. Geochemistry of subduction zone serpentinites: A review. Lithos 178, 96–127.
Deer, W., Howie, R., Zussman, J., 1992. An introduction to the rock forming minerals, Second Edition. Longman Scientific and Technical, London, p. 696.
Dick, H.J.B., Bullen, T., 1984. Chromian spinel as a petrogenetic indicator in abyssal and alpine-type peridotites and spatially associated lavas. Contrib. Miner. Petrol. 86, 54–76.
Dick, H.J.B., Natland, J.H., 1996. Late-stage melt evolution and transport in the shallow mantle beneath the East Pacific Rise, in Gullis, K., Mevel, C., Allan, J. (Eds.), Proceeding of the Ocean Drilling Program Scientific Results 147.Ocean Drilling Program, College Station, TX, pp. 103–134.
Dilek, Y., Ahmed, Z., 2003. Proterozoic ophiolites of the Arabian Shield and their significance in Precambrian tectonics, in Dilek, Y. and Robinson, P.T. (Eds.) Ophiolites in Earth History. Geological Society of London Special Publication 218, 685–700.
Dilek, Y., Robinson, P., 2003. Ophiolites in Earth history: Introduction. Geol. Soc., Lond., Spec. Publ. No. 218 (1), 1–8.
Dilek, Y., Furnes, H., Shallo, M., 2008. Geochemistry of the Jurassic Mirdita Ophiolite (Albania) and the MORB to SSZ evolution of a marginal basin oceanic crust. Lithos 100 (1–4), 174–209.
Dilek, Y., Thy, P., 2009. Island arc tholeiite to boninitic melt evolution of the Cretaceous Kizildag (Turkey) ophiolite: Model for multi-stage early arc–forearc magmatism in Tethyan subduction factories. Lithos 113 (1–2), 68–87.
Dilek, Y., Furnes, H., 2011. Ophiolite genesis and global tectonics: Geochemical and tectonic fingerprinting of ancient oceanic lithosphere. Geol. Soc. Am. Bull. 123 (3–4), 387–411.
Dilek, Y., Furnes, H., 2014. Ophiolites and Their Origins. Elements 10 (2), 93–100.
Dourgham, I.A., Fawzy, K.M., Frimmel, H.E., 2017. Ore minerals and geochemical characterization of the Dungash gold deposit, South Eastern Desert, Egypt. Arab. J. Geosci. 10 (6), 145.
Dungan, M.A., 1979. A microprobe study of antigorite and some serpentine pseudomorphs. Can. Mineral. 17, 771–784.
Edwards, S.J., Pearce, J.A., Freeman, J., 2000. New insights concerning the influence of water during the formation of podiform chromite, in Dilek, Y., Moores, E.M., Elthon, D., Nicolas, A. (Eds.), Ophiolites and Oceanic Crust: New insights from Field Studies and the Ocean Drilling Program. Boulder, Colorado: Geological Society of America Special Paper 349, 139–147. Contribution to Mineralogy and Petrology 96, 357–370.
El-Sayed, M., Furnes, H., Mohamed, F., 1999. Geochemical constraints on the tectonomagmatic evolution of the late Precambrian Fawakhir ophiolite, Central eastern Desert, Egypt. J. African Earth Sci. 29, 515–533.
Evans, B.W., 2010. Lizardite vs. antigorite serpentinite: magnetite, hydrogen, and life (?). Geology 38, 879–882.
Evans, B.W., Frost, B.R., 1975. Chrome-spinel in progressive metamorphism - a preliminary analysis. Geochim. Cosmochim. Acta 39, 959–972.
Farahat, E.S., El Mahalawi, M.M., Hoinkes, G., Abdel Aal, A.Y., 2004. Continental back-arc basin origin of some ophiolites from the Eastern Desert of Egypt. Contrib. Miner. Petrol. 82, 81–104.

Farahat, E.S., 2008. Chrome-spinels in serpentinites and talc carbonates of the El Ideid-El-Sodmein District, central Eastern Desert, Egypt: their metamorphism and petrogenetic implications. Chem. Erde 68, 193–205.
Frost, B.R., 1991. Stability of oxide minerals in metamorphic rocks, in Lindsley, D.H. (Ed.), Oxide Minerals: Their Petrologic and Magnetic Significance, Washington, DC: Mineralogical Society of America, Reviews in Mineralogy 25, pp. 469–488.
Gahlan, H.A., Azer, M.K., Khalil, A.E.S., 2015. The Neoproterozoic Abu Dahr ophiolite, South Eastern Desert, Egypt: petrological characteristics and tectonomagmatic evolution. Mineral. Petrol. 109 (5), 611–630.
Gahlan, H.A., Azer, M.K., Asimow, P.D., 2018. On the relative timing of listvenite formation and chromian spinel equilibration in serpentinites. Am. Mineral. 103 (7), 1087–1102.
Gahlan, H.A., Azer, M.K., Asimow, P.D., Mubarak, H.S., Al-Kahtany, K.M., 2020a. Petrological characteristics of the Neoproterozoic Ess ophiolite mantle section, Arabian Shield, Saudi Arabia: a mineral chemistry perspective. Int. J. Earth Sci. 109, 239–251.
Gahlan, H.A., Azer, M.K., Asimow, P.D., Al-Kahtany, K.M., 2020b. Genesis and geodynamic evolution of serpentinized ultramafics and the associated magnesite deposits, Al-Wask ophiolite, Arabian Shield, Saudi Arabia. Am. J. Sci. 320, 236–279.
Gahlan, H.A., Azer, M.K., Al-Kahtany, K., M.,, 2021. Petrogenesis and geodynamic setting of high-Cr chromitites in fore-arc peridotites: A case study from the Halaban ophiolite, Eastern Arabian Shield, Saudi Arabia. Lithos 396–397, 106243.
Gamal El Dien, H., Hamdy, M., Abu El-Ela, A.S., Abu-Alam, T., Hassan, A., Kil, Y., Mizukami, T., Soda, Y., 2016. Neoproterozoic serpentinites from the Eastern Desert of Egypt: Insights into Neoproterozoic mantle geodynamics and processes beneath the Arabian-Nubian Shield. Precambr. Res. 286, 213–233.
Gamal El Dien, H., Arai, S., Doucet, L.-S., Li, Z.-X., Kil, Y., Fougerouse, D., Reddy, S.M., Saxey, D.W., Hamdy, M., 2019. Cr-spinel records metasomatism not petrogenesis of mantle rocks. Nat. Commun. 10 (1), 1–12.
Gasparik, T., 1987. Orthopyroxene thermobarometry in simple and complex systems. Contrib. Miner. Petrol. 96, 357–370.
Ghiorso, M.S., Sack, R.O., 1995. Chemical mass transfer in magmatic processes IV. a revised and internally consistent thermodynamic model for the interpolation and extrapolation of liquid-solid equilibria in magmatic systems at elevated temperatures and pressures. Contrib. Miner. Petrol. 119, 197–212.
Girardeau, J., Mevel, C., 1982. Amphibolitized sheared gabbros from ophiolites as indicators of the evolution of the oceanic crust: Bay of Islands, Newfoundland. Earth Planet. Sci. Lett. 61, 151–165.
Godard, M., Lagabrielle, Y., Alard, O., Harvey, J., 2008. Geochemistry of the highly depleted peridotite drilled at ODP Sites 1272 and 1274 (Fifteen-Twenty Fracture Zone, Mid-Atlantic Ridge): Implications for mantle dynamics beneath a slow spreading ridge. Earth Planet. Sci. Lett. 267 (3–4), 410–425.
González-Jiménez, J.M., Proenza, J.A., Gervilla, F., Melgarejo, J.C., Blanco-Moreno, J.A., Ruiz-Sanchez, R., Griffin, W.L., 2011. High-Cr and high-Al chromitites from the Sagua de Tánamo District, Mayarí-Cristal ophiolitic massif (eastern Cuba): Constraints on their origin from mineralogy and geochemistry of chromian spinel and platinum-group elements. Lithos 125, 101–121.
González-Jiménez, J.M., Griffin, W.L., Proenza, J.A., Gervilla, F., O'Reilly, S.Y., Akbulut, M., Pearson, N.J., Arai, S., 2014. Chromitites in ophiolites: How, where, when, why? Part II. The crystallization of chromitites. Lithos 189, 140–158.
Griffin, W.L., Afonso, J.C., Belousova, E.A., Gain, S.E., Gong, X.-H., González-Jiménez, J. M., Howell, D., Huang, J.-X., McGowan, N., Pearson, N.J., Satsukawa, T., Shi, R., Williams, P., Xiong, Q., Yang, J.-S., Zhang, M., O'Reilly, S.Y., 2016. Mantle recycling: Transition zone metamorphism of Tibetan ophiolitic peridotites and its tectonic implications. J. Petrol. 57 (4), 655–684.
Habtoor, A.M., Ahmed, A.H., Akizawa, N., Harbi, H., Arai, S., 2017. Chemical homogeneity of high-Cr chromitites as indicator for widespread invasion of boninitic melt in mantle peridotite of Bir Tuluha ophiolite, Northern Arabian Shield, Saudi Arabia. Ore Geol. Rev. 90, 243–259.
Hart, S.R., Zindler, A., 1986. In search of a bulk-Earth composition. Chem. Geol. 57 (3–4), 247–267.
Hattori, K., Takahashi, V., Guillet, S., Johanson, B., 2005. Occurrence of arsenic (V) in forearc mantle serpentinites based on X-ray absorption spectroscopy study. Geochim. Cosmochim. Acta 69, 5585–5596.
Hawthorne, F.C., Oberti, R., Harlow, G.E., Maresch, W.V., Martin, R.F., Schumacher, J. C., Welch, M.D., 2012. IMA report, nomenclature of the amphibole supergroup. Am. Mineral. 97, 2031–2048.
Helba, H.A., Khalil, K.I., Abou, N.M.F., 2001. Alteration Patterns Related to Hydrothermal Gold Mineralizaition in Meta-andesites at Dungash Area, Eastern Desert. Egypt. Resour. Geol. 51 (1), 19–30.
Hey, M.H., 1954. A new review of the chlorites. Mineral. Mag. 30, 277–292.
Hirose, K., Kawamoto, T., 1995. Hydrous partial melting of lherzolite at 1 GPa: the effect of H_2O on the genesis of basaltic magmas. Earth Planet. Sci. Lett. 133, 463–473.
Hussein, A., Mazhar, A., Smith, M., Masoud, M., Khyamy, A., Hamouda, E., Moussa, M., 1996. Geological map of Ghadir-Dunqash district, Eastern Desert, Egypt. Egyptian Geological Survey, Egypt.
Ishii, T., Robinson, P.T., Maekawa, H., Fiske, R., 1992. Petrological studies of peridotites from diapiric serpentinite seamounts in the Izu-Ogasawara-Mariana forearc, leg 125, in Fryer, P., Pearce, J.A., Stokking, L. B. et al. (Eds), Proceedings of the Ocean Drilling Program. Scientific Results 125, 445–485.
Jackson, E.D., Thayer, T.P., 1972. Some criteria for distinguishing between stratiform, concentric and alpine peridotite-gabbro complexes. 24th International Geological Congress 2, 297–302.
Jagoutz, E., Palme, H., Baddenhausen, H., Blum, K., Cendales, M., Dreibus, G., Spettel, B., Lorenz, V., Wänke, H., 1979. The abundances of major, minor and trace elements in the earth's mantle as derived from primitive ultramafic nodules. Geochim. Cosmochim. Acta 11 (2), 2031–2050.
Jan, M.Q., Windley, B.F., 1990. Chromian spinel silicate chemistry in ultramafic rocks of the Jijal Complex, northwestern Pakistan. J. Petrol. 31, 667–715.
Johnson, P.R., Kattan, F.H., Al-Saleh, A.M., 2004. Neoproterozoic ophiolites in the Arabian Shield: Field relations and structure. Develop. Precambr. Geol. 13, 129–162.
Kamenetsky, V.S., Crawford, A.J., Meffre, S., 2001. Factors controlling chemistry of magmatic spinel: An empirical study of associated olivine, Cr-spinel and melt inclusions from primitive rocks. J. Petrol. 42, 655–671.
Kapsiotis, A., Tsikouras, B., Grammatikopoulos, T., Karipi, S., Hatzipanagiotou, K., 2007. On the metamorphic modification of Cr-spinel compositions from the ultrabasic rocks of the Pindos ophiolite complex (NW Greece). Bull. Geol. Soc. Greece 40 (2), 781–793.
Kapsiotis, A., 2014. Composition and alteration of Cr-spinels from Milia and Pefki serpentinized mantle peridotites (Pindos Ophiolite Complex, Greece). Geol. Carpath. 65 (1), 83–95.
Kassem, O.M.K., Abd El Rahim, S.H., 2014. Finite strain analysis of metavolcanics and metapyroclastics in gold-bearing shear zone of the Dungash area, Central Eastern Desert, Egypt. Geotectonics 48 (6), 483–495.
Kassem, O.M.K., Abd El Rahim, S.H., El Nashar, E.S.R., Al Kahtany, K.M., 2016. Application of kinematic vorticity and gold mineralization for the wall rock alterations of shear zone at Dungash gold mining, Central Eastern Desert, Egypt. Geol. Ore Deposits 58 (6), 499–515.
Keeditse, M., Rajesh, H.M., Belyanin, G.A., Fukuyama, M., Tsunogae, T., 2016. Primary magmatic amphibole in Archaean meta-pyroxenite from the central zone of the Limpopo Complex, South Africa. S. Afr. J. Geol. 119 (4), 607–622.
Khalid, A., El Naggar, A., Bakhit, H., 1987. Results of detailed exploration work on Dungash area. Internal report, Geological Survey of Egypt, Cairo, Egypt.
Khalil, K.I., 2007. Chromite mineralization in ultramafic rocks of the Wadi Ghadir area, Eastern Desert, Egypt: Mineralogical, microchemical and genetic studies. Neues Jahrbuch für Mineralogie - Abhandlungen. 183, 283–296.
Khalil, K.I., Helba, H.A., Mücke, A., 2003. Genesis of the gold mineralization at the Dungash gold mine area, Eastern Desert, Egypt: a mineralogical–microchemical study. J. Afr. Earth Sc. 37 (1–2), 111–122.
Khalil, A.E.S., Azer, M.K., 2007. Supra-subduction affinity in the Neoproterozoic serpentinites in the Eastern Desert, Egypt: evidence from mineral composition. J. Afr. Earth Sc. 49, 136–152.
Khalil, A.E.S., Obeid, M.A., Azer, M.K., 2014. Serpentinized Peridotites at the North Part of the Wadi Allaqi District (Egypt): Implications for the Tectono-Magmatic Evolution of Fore-arc Crust. Acta Geologica Sinica-English Edition 88 (5), 1421–1436.
Khedr, M.Z., Arai, S., 2016. Petrology of a Neoproterozoic Alaskan-type complex from the Eastern Desert of Egypt: implications for mantle heterogeneity. Lithos 263, 15–32.
Khedr, M.Z., Arai, S., 2017. Peridotite-chromitite complexes in the Eastern Desert of Egypt: Insight into Neoproterozoic sub-arc mantle processes. Gondwana Res. 52, 59–79.
Klemm, D., Klemm, R., Murr, A., 2001. Gold of the Pharaohs–6000 years of gold mining in Egypt and Nubia. J. Afr. Earth Sc. 33 (3–4), 643–659.
Kusky, T.M., Ramadan, T.M., 2002. Structural controls on Neoproterozoic mineralization in the South Eastern Desert, Egypt: an integrated field, Landsat TM, and SIR-C/X SAR approach. J. Afr. Earth Sc. 35 (1), 107–121.
Lago, B., Rabinowicz, M., Nicolas, A., 1982. Podiform chromite ore bodies: a genetic model. J. Petrol. 23, 103–125.
Lapham, D.M., 1958. Structural and chemical variation in chromium chlorite. Am. Mineral. 43 (9–10), 921–956.
Leng, W., Gurnis, M.C., Asimow, P.D., 2012. From basalts to boninites: the geodynamics of volcanic expression during induced subduction initiation. Lithosphere 4 (6), 511–523.
Matveev, S., Balhaus, C., 2002. Role of water in the origin of podiform chromitite deposits. Earth Planet. Sci. Lett. 203, 235–243.
McCormick, G.R., 1975. A chemical study of kämmererite, Day Book Body, Yancey Country, North Carolina. Am. Mineral. 60, 924–927.
McDonough, W.F., Sun, S.S., 1995. Composition of the Earth. Chem. Geol. 120, 223–253.
McElduff, B., Stumpfl, E.F., 1991. The chromite deposits of the Troodos complex, Cyprus— evidence for the role of a fluid phase accompanying chromite formation. Miner. Deposita 26, 307–318.
Melcher, F., Grum, W., Thalhammer, T.V., Thalhammer, O.A.R., 1999. The giant chromite deposits at Kempirsai, Urals: constraints from trace element (PGE, REE) and isotope data. Miner. Deposita 34 (3), 250–272.
Mellini, M., Rumori, C., Viti, C., 2005. Hydrothermally reset magmatic spinels in retrograde serpentinites: formation of "ferritchromite" rims and chlorite aureoles. Contrib. Miner. Petrol. 149 (3), 266–275.
Merlini, A., Grieco, G., Diella, V., 2009. Ferritchromite and chromian-chlorite formation in mélange-hosted Kalkan chromitite (Southern Urals, Russia). Am. Mineral. 94, 1459–1467.
Miura, M., Arai, S., Ahmed, A.H., Mizukami, T., Okuno, M., Yamamoto, S., 2012. Podiform chromitite classification revisited: a comparison of discordant and concordant chromitite pods from Wadi Hilti, northern Oman ophiolite. J. Asian Earth Sci. 59, 52–61.
Mondal, S.K., Ripley, E.M., Li, C., Frei, R., 2006. The genesis of Archaean chromitites from the Nuasahi and Sukinda massifs in the Singhbhum Craton, India. Precambr. Res. 148, 45–66.
Moody, J.B., 1976. Serpentinization: a review. Lithos 9, 125–138.
Morimoto, N., Fabries, J., Ferguson, A.K., Ginzburg, I.V., Ross, M., Seifert, F.A., Zussman, J., Aoki, K., Gottardi, G., 1988. Nomenclature of pyroxenes. Mineral. Mag. 52, 535–550.

Morishita, T., Andal, E., Arai, S., Ishida, Y., 2006. Podiform chromitites in lherzolite dominant mantle section of Isabela ophiolite, Philippines. Isl. Arc 15, 80–101.
Moussa, H.E., Azer, M.K., Abou El Maaty, M.A., Maurice, A.E., Yanni, N.N., Akarish, A.I., Elnazer, A.A., Elsagheer, M.A., 2021. Carbonation of Neoproterozoic mantle section and formation of gold-bearing listvenite in the Northern Nubian Shield. Lithos 406–407, 106525.
Mubarak, H.S., Azer, M.K., Surour, A.A., Moussa, H.E., Asimow, P.D., Kabesh, M.M.L., 2020. Mineralogical and geochemical study of rodingites and associated serpentinized peridotite, Eastern Desert of Egypt. Arabian-Nubian Shield. Lithos 374–375, 105720.
Murck, B.W., Campbell, I.H., 1986. The effect of temperature, oxygen fugacity and melt composition on the behavior of chromium in basic and ultrabasic melts. Geochim. Cosmochim. Acta 50, 1871–1887.
Niu, Y.L., 2004. Bulk-rock major and trace element compositions of abyssal peridotites: Implications for mantle melting, melt extraction and post-melting processes beneath mid-ocean ridges. J. Petrol. 38, 1047–1074.
Obeid, M.E., Khalil, A.E.S., Azer, M.K., 2016. Mineralogy, geochemistry, and geotectonic significance of the Neoproterozoic ophiolite of Wadi Arais area, south Eastern Desert, Egypt. Int. Geol. Rev. 58 (6), 687–702.
Ohara, Y., Stern, R.J., Ishii, T., Yurimoto, H., Yamazaki, T., 2002. Peridotites from the Mariana Trough: first look at the mantle beneath an active back-arc basin. Contrib. Miner. Petrol. 143, 1–18.
Olivier, N., Boyet, M., 2006. Rare earth and trace elements of microbialites in Upper Jurassic coral-and sponge-microbialite reefs. Chem. Geol. 230, 105–123.
Pagé, P., Bédard, J., Schroetter, J., Tremblay, A., 2008. Mantle petrology and mineralogy of the Thetford Mines ophiolite complex. Lithosphere 100, 255–292.
Paktunc, A.D., 1990. Origin of podiform chromite deposits by multistage melting, melt segregation and magma mixing in upper mantle. Ore Geol. Rev. 5, 211–222.
Pal, T., Mitra, S., 2004. *P-T-fO*$_2$ controls on a partly inverse chromite-bearing ultramafic intrusive: an evaluation from the Sukinda Massif, India. J. Asian Earth Sci. 22, 483–493.
Pallister, J.S., Stacey, J.S., Fischer, L.B., Premo, W.R., 1988. Precambrian ophiolites of Arabia: Geologic settings, U-Pb geochronology, Pb-isotope characteristics, and implications for continental accretion. Precambr. Res. 38, 1–54.
Parkinson, I.J., Pearce, J.A., 1998. Peridotites from the Izu-Bonin-Mariana forearc (ODP Leg 125): Evidence for mantle melting and melt-mantle interaction in a supra-subduction zone setting. J. Petrol. 39 (9), 1577–1618.
Paulick, H., Bach, W., Godard, M., De Hoog, J.C.M., Suhr, G., Harvey, J., 2006. Geochemistry of abyssal peridotites (Mid-Atlantic Ridge, 15°20′ N, ODP Leg 209): Implications for fluid/rock interaction in slow spreading environments. Chem. Geol. 234, 179–210.
Pearce, J.A., Barker, P.F., Edwards, S.J., Parkinson, I.J., Leat, P.T., 2000. Geochemistry and tectonic significance of peridotites from the South Sandwich arc-basin system, South Atlantic. Contrib. Miner. Petrol. 139, 36–53.
Purvis, A., Nesbitt, R., Halberg, J., 1972. The geology of part of Carr Boyd Complex and its associated nickel mineralization, Western Australia. Econ. Geol. 67, 10931113.
Richard, L.R., 1995. Mineralogical and petrological data processing system. Minpet Software (c) 1988-1995, Version 2.02.
Roberts, S., 1988. Ophiolitic chromitite formation: a marginal basin phenomenon? Econ. Geol. 83, 1034–1036.
Rollinson, H., 2005. Chromite in the mantle section of the Oman ophiolite: a new genetic model. Isl. Arc 14, 542–550.
Saka, S., Uysal, T., Akmaz, R., Kaliwoda, M., Hochleitner, R., 2014. The effect of partial melting, melt-mantle interaction and fractionation on ophiolite generations: constraints from the Cretaceous Pozantı-Karsantı ophiolite, southern Turkey. Lithos 202, 300–316.
Salem, S.M., El Sharkawi, M., El-Alfy, Z., Soliman, N.M., Ahmed, S.E., 2016. Exploration of gold occurrences in alteration zones at Dungash district, Southeastern Desert of Egypt using ASTER data and geochemical analyses. J. Afr. Earth Sc. 117, 389–400.
Scambelluri, M., Cannaò, E., Gilio, M., 2019. The water and fluid-mobile element cycles during serpentinite subduction. A review. Eur. J. Mineral. 31, 405–428.
Sepidbar, F., Lucci, F., Biabangard, H., Zaki Khedr, M., Jiantang, P., 2020. Geochemistry and tectonic significance of the Fannuj-Maskutan SSZ-type ophiolite (Inner Makran, SE Iran). Int. Geol. Rev. 62 (16), 2077–2104.
Shackleton, R.M., 1994. Review of late Proterozoic sutures, ophiolitic mélanges and tectonics of eastern Egypt and northeastern Sudan. Geol. Rundsch. 83, 537–546.
Stern, R.J., Johnson, P.R., Kröner, A., Yibas, B., 2004. Neoproterozoic ophiolites of the Arabian-Nubian Shield. In: Kusky, T.M. (Ed.), Precambrian Ophiolites and Related Rocks. Developments in Precambrian Geology 13, 95–128. Amsterdam: Elsevier.
Stolper, D.A., Bucholz, C.E., 2019. Neoproterozoic to early Phanerozoic rise in island arc redox state due to deep ocean oxygenation and increased marine sulfate levels. Proc. Natl. Acad. Sci. 116 (18), 8746–8755.
Stowe, C.W., 1994. Compositions and tectonic settings of chromite deposits through time. Econ. Geol. 89 (3), 528–546.
Suita, M.T.F., Strieder, A.J., 1996. Cr-spinels from Brazilian mafic-ultramafic complexes: metamorphic modifications. Int. Geol. Rev. 38 (3), 245–267.
Thalhammer, O.A.R., Prochaska, W., Mühlhans, H.W., 1990. Solid inclusions in chrome-spinels and platinum group element concentrations from the Hochgrössen and Kraubath Ultramafic Massifs (Austria). Contrib. Miner. Petrol. 105, 66–80.
Uysal, İ., Kaliwoda, M., Karsli, O., Tarkian, M., Sadiklar, M.B., Ottley, C.J., 2007. Compositional variations as a result of partial melting and melt–peridotite interaction in an upper mantle section from the Ortaca area, southwestern Turkey. Can. Mineralogist 45 (6), 1471–1493.
Uysal, İ., Ersoy, E., Dilek, Y., Kapsiotis, A., Sarıfakıoğlu, E., 2016. Multiple episodes of partial melting, depletion, metasomatism and enrichment processes recorded in the heterogeneous upper mantle sequence of the Neotethyan Eldivan ophiolite, Turkey. Lithos 246, 228–245.
Whittaker, E.J., Wicks, F.J., 1970. Chemical differences among the serpentine "polymorphs": a discussion. Am. Mineral. 55, 1025–1047.
Workman, R.K., Hart, S.R., 2005. Major and trace element composition of the depleted MORB mantle (DMM). Earth Planet. Sci. Lett. 231 (1–2), 53–72.
Wu, W., Yang, J., Wirth, R., Zheng, J., Lian, D., Qui, T., Milushi, I., 2019. Carbon and nitrogen isotopes and mineral inclusions in diamonds from chromitites of the Mirdita ophiolite (Albania) demonstrate recycling of oceanic crust into the mantle. Am. Mineral. 104 (4), 485–500.
Xiong, F., Yang, J., Dilek, Y., Wang, C., Hao, X., Xu, X., Lian, D., 2017. Petrology and geochemistry of the high-Cr podiform chromitites of the Köycegiz ophiolite, southwest Turkey: implications for the multi-stage evolution of the oceanic upper mantle. Mineral. Petrol. 112 (5), 685–704.
Xiong, F., Yang, J., Dilek, Y., Wang, C., Hao, X., Xu, X., Lian, D., 2018. Petrology and geochemistry of the high-Cr podiform chromitites of the Köycegiz ophiolite, southwest Turkey: implications for the multi-stage evolution of the oceanic upper mantle. Mineral. Petrol. 112, 685–704.
Yamamoto, S., Nakajima, J., Hasegawa, A., Maruyama, S., 2009. Izu-Bonin arc subduction under the Honshu island, Japan: Evidence from geological and seismological aspect. Gondwana Res. 16 (3–4), 572–580.
Yang, J., Ming, F., Xu, X., Robinson, P.T., Dilek, Y., Makeyev, A.B., Wirth, R., Wiedenbeck, M., Cliff, J., 2015. Diamonds, native elements and metal alloys from chromitites of the Ray-Iz ophiolite of the Polar Urals. Gondwana Res. 27 (2), 459–485.
Zhou, M.F., Robinson, P.T., Bai, W.J., 1994. Formation of podiform chromitites by melt/rock interaction in the upper mantle. Miner. Deposita 29, 98–101.
Zhou, M.F., Robinson, P.T., Malpas, J., Li, Z., 1996. Podiform chromitites in the Luobusa ophiolite (southern Tibet): implications for melt-rock interaction and chromite segregation in the upper mantle. J. Petrol. 37 (1), 3–21.
Zhou, M.F., Robinson, P.T., 1997. Origin and tectonic environment of podiform chromite deposits. Econ. Geol. 92, 259–262.
Zhou, M.F., Robinson, P.T., Malpas, J., Edwards, S.J., Qi, L., 2005. REE and PDE geochemical cnstraints on the formation of dunites in the Luobusa Ophiolite, Southern Tibet. J. Petrol. 46, 615–639.
Zimmer, M., Kröner, A., Jochum, K.P., Reischmann, T., Todt, W., 1995. The Gabal Gerf complex: a Precambrian N-MORB ophiolite in the Nubian shield, NE Africa. Chem. Geol. 123 (1–4), 29–51.
Zoheir, B., Weihed, P., 2014. Greenstone-hosted lode-gold mineralization at Dungash mine, Eastern Desert, Egypt. J. Afr. Earth Sci. 99, 165–187.
Zoheir, B.A., El-Shazly, A.K., Helba, H., Khalil, K.I., Bodnar, R.J., 2008. Origin and evolution of the Um Egat and Dungash orogenic gold deposits, Egyptian Eastern Desert: Evidence from fluid inclusions in quartz. Econ. Geol. 103 (2), 405–424.